Topographic signatures and a general transport law for deep-seated landslides in a landscape evolution model

Adam M. Booth,[1] Josh J. Roering,[2] and Alan W. Rempel[2]

Received 10 August 2012; revised 19 February 2013; accepted 21 February 2013; published 14 May 2013.

[1] A fundamental goal of studying earth surface processes is to disentangle the complex web of interactions among baselevel, tectonics, climate, and rock properties that generate characteristic landforms. Mechanistic geomorphic transport laws can quantitatively address this goal, but no widely accepted law for landslides exists. Here we propose a transport law for deep-seated landslides in weathered bedrock and demonstrate its utility using a two-dimensional numerical landscape evolution model informed by study areas in the Waipaoa catchment, New Zealand, and the Eel River catchment, California. We define a non-dimensional landslide number, which is the ratio of the horizontal landslide flux to the vertical tectonic flux, that characterizes three distinct landscape types. One is dominated by stochastic landsliding, whereby discrete landslide events episodically erode material at rates exceeding the long-term uplift rate. Another is characterized by steady landsliding, in which the landslide flux at any location remains constant through time and is greatest at the steepest locations in the catchment. The third is not significantly affected by landsliding. In both the "stochastic landsliding" and "steady landsliding" regimes, increases in the non-dimensional landslide number systematically reduce catchment relief and widen valley spacing, producing long, low angle hillslopes despite high uplift rates. The stochastic landsliding regime captures the frequent observation that deep-seated landslides produce large sediment fluxes from small areal extents while being active only a fraction of the time. We suggest that this model is adaptable to a wide range of geologic settings and is useful for interpreting climate-driven changes in landslide behavior.

Citation: Booth, A. M., J. J. Roering, and A. W. Rempel (2013), Topographic signatures and a general transport law for deep-seated landslides in a landscape evolution model, *J. Geophys. Res. Earth Surf.*, *118*, 603–624, doi:10.1002/jgrf.20051.

1. Introduction

[2] The topographic characteristics of a drainage basin are governed by complex interactions among various hillslope and channel processes, which in turn are sensitive to changes in baselevel, climate, and rock properties. A fundamental goal of studying earth surface processes is to disentangle this complex web of interactions in order to quantitatively relate observed topographic forms to the underlying geomorphic processes [*National Research Council*, 2010]. Such quantitative relationships are required in order to infer previous drivers of landscape evolution based on current landscape characteristics, as well as to predict how landscapes will respond to changes in these drivers.

[3] A common approach for making such interpretations or predictions is to utilize geomorphic transport laws, which give sediment fluxes or incision rates based on topographic attributes, such as slope or drainage area, as well as material properties, such as bulk density or material strength [*Dietrich et al.*, 2003]. Ideally, these laws derive from simple mechanistic principles, and field, experimental, and mathematical modeling studies support their utility. Several geomorphic transport laws have been proposed and proven useful for studies of landscape evolution, including soil transport on hillslopes [*Culling*, 1960; *Roering et al.*, 1999], soil production from bedrock [*Heimsath et al.*, 1997], and detachment-limited river incision [*Howard and Kerby*, 1983]. However, many other geomorphic processes lack established transport laws, especially those processes with rates and basic properties that vary dramatically over wide ranges of temporal and spatial scales. This paper focuses on one of these processes: deep-seated landslides, which we define here as extending to the depth of the lowermost weathering front.

[4] Landslides with sizes and rates of movement spanning many orders of magnitude are the dominant erosion process in many catchments where erosion rates are high (greater than ~1 mm yr^{-1}). The topography often manifests this process dominance through uniformly high relief and steep topographic gradients, or threshold hillslopes, which are insensitive to changes in uplift rate [*Schmidt and Montgomery*, 1995; *Burbank et al.*, 1996; *Montgomery and Brandon*, 2002] but can differ among bedrock types [*Korup*, 2008] and with climate [*Gabet et al.*, 2004]. Erosion rates derived

[1]California Institute of Technology, Division of Geological and Planetary Sciences, Pasadena, California, USA.
[2]University of Oregon, Department of Geological Sciences, Eugene, Oregon, USA.

Corresponding author: A. M. Booth, California Institute of Technology, Division of Geological and Planetary Sciences, MC 170–25, 1200 E. California Blvd., Pasadena, CA 91125, USA. (bootha@caltech.edu)

2169-9003/13/10.1002/jgrf.20051

from landslide frequency-size distributions confirm the importance of landsliding, which can keep pace with or even exceed the tectonic uplift rate [*Hovius et al*., 1997, 2011; *Malamud et al*., 2004; *Blodgett and Isacks*, 2007; *Parker et al*., 2011; *Larsen and Montgomery*, 2012]. These studies focused on some of the world's highest mountain ranges, with thousands of meters of relief, but many other regions have high erosion rates and only modest topographic relief of hundreds of meters [*Griffiths*, 1982; *Milliman and Syvitski*, 1992]. We note that many of these settings are commonly underlain by mechanically weak bedrock that is especially prone to weathering and deep-seated landsliding. Deep-seated landslides keep pace with rapid uplift rates by providing a large flux of sediment from a small area [*Kelsey*, 1978; *Mackey and Roering*, 2011], but little is known about how this process plays out at longer than historic timescales over which drainage basins evolve. Figure 1 provides one snapshot of such a landscape from the Waipaoa catchment, North Island, New Zealand, where Holocene erosion rates are 3–4 mm yr^{-1} [*Berryman et al*., 2000] and deep-seated landslides abound.

[5] Despite the known importance of landslides to landscape evolution in a variety of settings, a geomorphic transport law for deep-seated landslides that can be straightforwardly implemented in a two-dimensional landscape evolution model remains elusive. *Ahnert* [1976, 1977] made a significant early attempt by including a plastic flow term, which was a function of weathering depth and the land surface slope, in a landscape evolution model, but explored only a limited range of model parameters. Later, *Kirkby* [1987] also developed a general model for mass movements but explored only topographic profiles. *Hergarten and Neugebauer* [1998, 1999] demonstrated that a landslide flux depending on both depth and slope could produce stochastic landslide behavior consistent with the theory of self-organized criticality [*Bak et al*., 1988]. Numerous models have invoked a threshold topographic gradient to simulate bedrock landsliding but arbitrarily deposited the material removed from slopes exceeding the threshold at downslope locations [*Tucker and Bras*, 1998; *van der Beek and Braun*, 1999; *Dadson and Church*, 2005]. To date, *Densmore et al*. [1998] have included the most realistic treatment of deep-seated landsliding in a landscape evolution model by assigning a probability of failure to each grid cell in a model landscape based on a mechanistically determined critical hillslope height. Failed material was deposited in the valley network, where it could experience feedbacks with channel processes. Despite this rather detailed treatment of landsliding, however, the choices of failure probability and deposit geometry were arbitrary and not relevant to moderate relief catchments dominated by deep-seated landsides.

[6] Here we propose a general transport law for a range of deep-seated landslide processes motivated by observations of sites on the north island of New Zealand and the northern

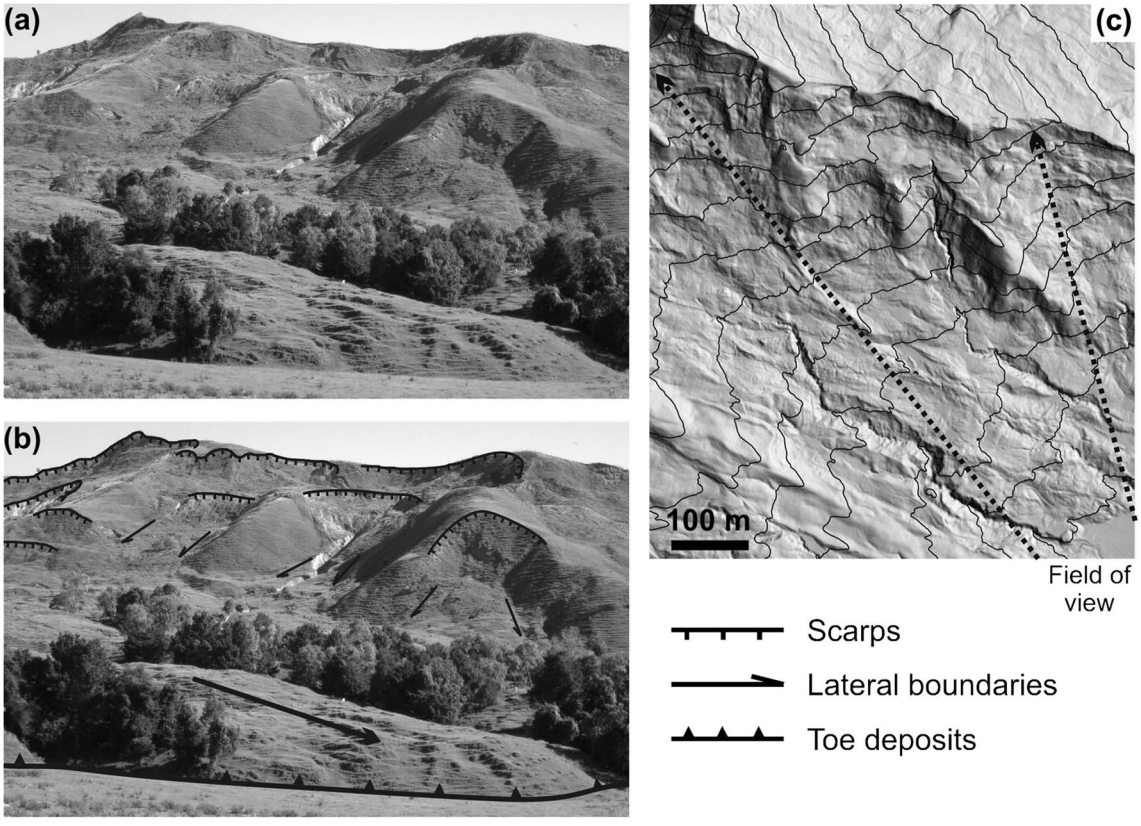

Figure 1. (a) Example of a catchment dominated by slow-moving, deep-seated landslides near the Waipaoa River, North Island, New Zealand (~ 38.34°S and 177.93°E, indicated in Figure 2). (b) The authors' interpretation of recent deep-seated landslide activity. Numerous scarps and landslide deposits exist amidst remnants of stable ridges. In the foreground, the individual landslides coalesce into a large, low gradient toe deposit. (c) Lidar-derived hillshade map of the area. Contour interval is 20 m, and the dashed arrows approximately indicate the field of view in Figures 1a and 1b.

California coast ranges of the United States. At these sites, we first use high-resolution topographic data to document a topographic signature of slow, deep-seated landslides. Motivated by empirical observations of vertical velocity profiles from deep-seated landslides throughout the world, we model landslides as non-Newtonian fluids so that landslide sediment flux depends nonlinearly on the landslide thickness and topographic gradient. Flow law parameters for a given site can be estimated from borehole inclinometer data. When combined with existing geomorphic transport laws for soil creep, channel incision, and bedrock weathering, modeled landslides systematically inhibit channel formation and reduce catchment-averaged topographic gradients to produce similar topographic signatures to those observed in the study areas. We document a rich variety of landscapes produced over a wide range of model parameters and show that a non-dimensional landslide number predicts the transition from stable, ridge-valley topography to landslide-dominated topography. The nature of this transition depends on the initial weathered zone thickness relative to the steady state thickness, which provides the mechanically weak material capable of generating landslides.

2. Topographic Signatures of Slow-Moving, Deep-Seated Landslides

[7] To motivate and inform our landscape evolution model, we first describe the geology and tectonic settings of two study sites with extensive deep-seated landsliding, one in the Waipaoa catchment, North Island, New Zealand, and the other along the Eel River, northern California, United States. We then use lidar-derived topographic data and slope-area statistics to document the topographic signatures of these deep-seated landslides.

2.1. Study Areas

[8] Our first study area is 160 km^2 situated just east of the Waipaoa River near Whatatutu, North Island, New Zealand (Figure 2). Bedrock there is mainly mudstone of Miocene to Pleistocene age [*Mazengarb and Speeden*, 2000]. The Miocene Tolaga Group rocks are most abundant and consist of undifferentiated, massive, thinly bedded, and slightly calcareous mudstones with rare sandstone, tuff, and conglomerate beds. Small regions underlain by either Pliocene mudstones and sandstones of the Mangaheia Group or Pleistocene sediments of the Mangatuna Formation exist in the southern part of the study area. In Figure 2 and throughout the text, we refer to these units collectively as mudstone. A melange of severely crushed Cretaceous to early Miocene lithologies in a sheared mudstone matrix underlies the northwestern part of the study area (Figure 2). The mudstone and melange portions of the study area both exhibit signs of widespread deep-seated landsliding, an example of which is shown in Figure 1. In the mudstone, deep-seated earthflows as well as shallow soil slips are common, while in the melange, earthflows are rampant and accompanied by minor gullying

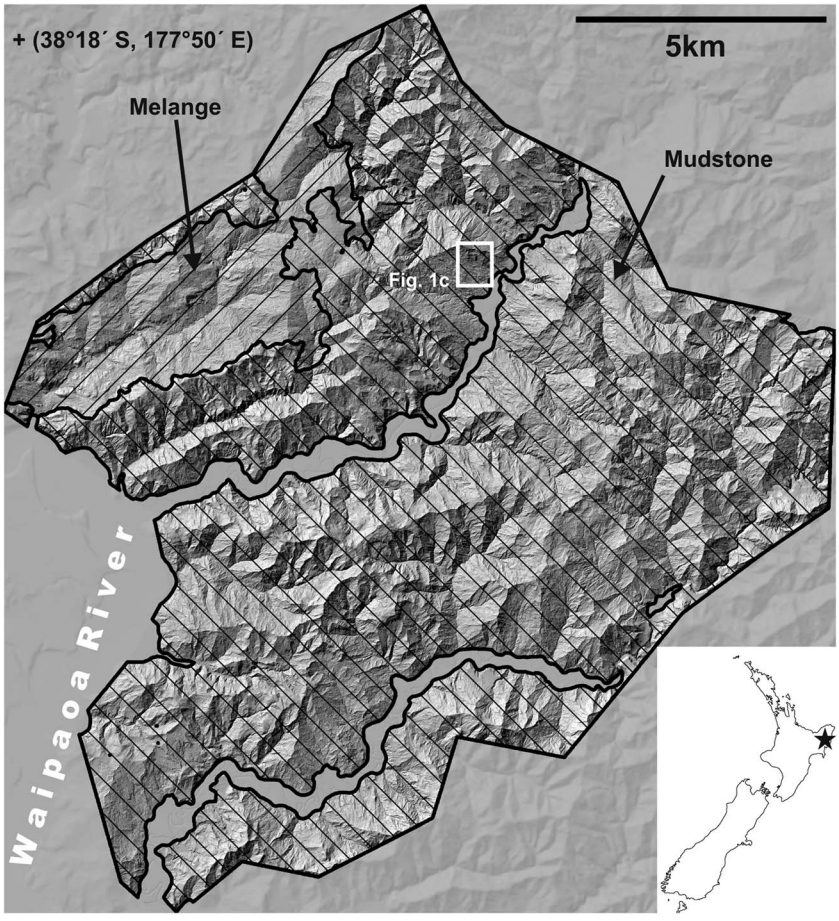

Figure 2. Lidar-derived hillshade map of the Waipaoa study area, with outlined geologic units used in the slope-area plot (Figure 4). White rectangle outlines the location of Figure 1.

[*Jessen et al*., 1999]. The New Zealand Land Resource Inventory Erosion Classification system [*Eyles*, 1985] defines each of these failure styles as follows: soil slips are rapid, shallow failures confined to less than 1 m below the surface, gullying removes soil or soft rock by the overland flow of water in narrow, ephemeral channels, and earthflows involve the flow of soil and underlying regolith while retaining a deforming surface cover. In our study area, earthflows commonly occur as deep-seated landslide complexes with soil slips and gully erosion occurring on the surface of the complex. Field reconnaissance indicates that the active deep-seated earthflows typically consist of well-mixed, clay-rich, weathered material with occasional logs and blocks of harder rock.

[9] The study site resides in a tectonically active region and has been experiencing rock uplift of ~0.7 mm yr^{-1} since the late Pleistocene, based on the deformation of aggradational terraces along the Waipaoa River [*Berryman et al*., 2000]. The elevation of the most recent terrace relative to the modern river indicates that the Waipaoa has incised at an average rate of 3–4 mm yr^{-1} over the past 18,000 years just to the west of our study area [*Berryman et al*., 2000]. Throughout the Waipaoa catchment, terraces and numerous knickpoints in tributary headwaters have decoupled areas of relict topography from this incision [*Crosby and Whipple*, 2006; *Gomez and Livingston*, 2012], but in our study area, this relict topography is relatively rare. Most of the mechanically weak slopes there have adjusted to the rapid decrease in baselevel through mass wasting processes [*Marden et al*., 2008].

[10] Our second study area is 180 km^2 along the main stem of the Eel River south of Alderpoint, California, United States (Figure 3). Bedrock there is the central belt of the Franciscan Complex, part of a metamorphosed and tectonically sheared Jurassic to Cretaceous accretionary prism [*McLaughlin et al*., 2000]. A highly sheared melange of meta-argillite with isolated blocks of chert, greenstone, and serpentinite underlies most of the northeastern part of the study area. In Figure 3, we delineate the widespread melange unit and exclude the largest of the chert, greenstone, and serpentinite blocks, such as in the northern portion of the study area. Metasandstone and meta-argillite of the Broken Formation underlie most of the southwestern part of the study area, and we refer to this unit simply as sandstone throughout the text. Deep-seated earthflows with irregular gully networks incised on their surfaces are common throughout the study area but especially abundant in the melange unit and transport material with surface velocities averaging ~0.4 m yr^{-1} [*Mackey and Roering*, 2011]. As in the Waipaoa study area, these earthflows transport weathered, clay-rich material with the occasional block of harder rock or other debris.

[11] This study area is actively uplifting due to its position relative to the northward migrating Mendocino Triple Junction [*Furlong and Govers*, 1999; *Furlong and Schwartz*, 2004]. Using a geodynamic model, *Lock et al*. [2006] estimated a current uplift rate of 0.5–1 mm yr^{-1} in our study area, which is similar to the modern, catchment-averaged erosion rate of ~0.9 mm yr^{-1} estimated from suspended sediment data near

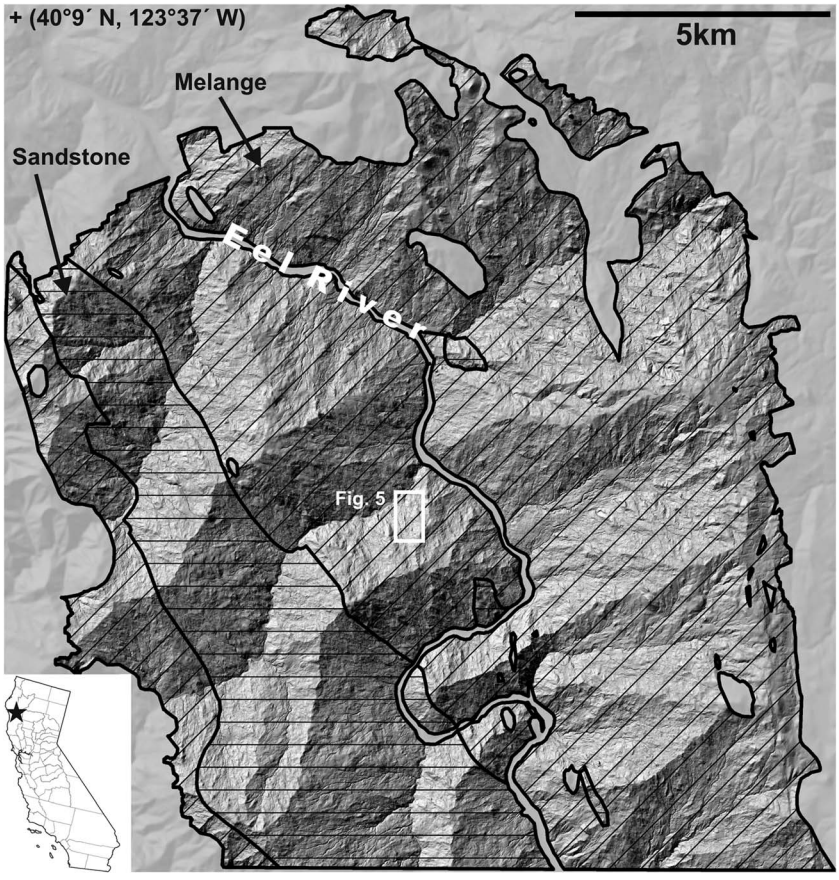

Figure 3. Lidar-derived hillshade map of the Eel River study area, with outlined geologic units used in the slope-area plot (Figure 4). White rectangle outlines the location of Figure 5.

the mouth of the Eel River [*Wheatcroft and Sommerfield*, 2005]. Earthflow movement alone is historically responsible for at least 0.45 mm yr^{-1} of erosion in the study area [*Mackey and Roering*, 2011].

[12] In both study areas, we used 2 m resolution bare earth digital elevation models (DEMs) derived from light detection and ranging (lidar) for our topographic analysis. NZ Aerial Mapping collected the lidar data for the Waipaoa site in 2010, and the National Center for Airborne Laser Mapping (NCALM) collected the Eel River lidar data in 2006.

2.2. Topographic Signatures

[13] Perhaps the most visually striking features of both study areas are the long, kilometer-scale, quasi-planar hillslopes. Clear examples of this topography are the ridges and valleys in the Waipaoa study area surrounding and immediately southeast of the white box in Figure 2, and the northeast trending ridges and valleys to the southwest of the Eel River in Figure 3. The gradient of these hillslopes is not controlled by rock structure in either study area, and instead, deep-seated landslides frequently span entire hillslopes from the ridge to the channel. This correspondence suggests that deep-seated landsliding might set this long hillslope length scale, a connection that we quantify below using slope-area statistics and slope distributions and then demonstrate with a mechanistic model in section 4.

[14] Slope-area plots, which document topographic gradient as a function of drainage area, are a standard tool for identifying the boundaries between geomorphic process regimes, such as the hillslope-valley transition [*Tarboton et al.*, 1991; *Montgomery and Foufoula-Georgiou*, 1993]. Figure 4a shows a slope-area plot for each main bedrock type in each of our study areas, along with plots from the Oregon Coast Range and Gabilan Mesa [*Roering et al.*, 2007], which lack deep-seated landslides, for reference. We computed drainage area in each 2×2 m grid cell using the D-infinity algorithm [*Tarboton*, 1997] and computed topographic gradient in the steepest downslope direction. This combination of drainage area and topographic gradient algorithms performed well on both hillslopes and channels in the study areas as well as in our modeled catchments, which allowed straightforward comparison of the study areas and model (section 4.5). Different drainage area and topographic gradient algorithms, for example, steepest descent and centered finite difference, respectively, reproduced the same process regimes described in the following paragraphs but resulted in more variability in the binned average trends.

[15] Despite differences in bedrock type, all four slope-area plots from the deep-seated landslide-prone lithologies exhibit similar trends in mean topographic gradient with increasing drainage area. In Figures 4 and 5, we identify four geomorphic process regimes, denoted by roman numerals I–IV, between each break in slope of the slope-area plot, and illustrate the spatial pattern of these regimes. At small drainage areas (regime I), slope increases rapidly until a drainage area of ~20 m^2. These grid cells correspond to stable ridge tops as well as scarps and hummocks on the surfaces of active and relict deep-seated landslides (Figure 5, pale yellow

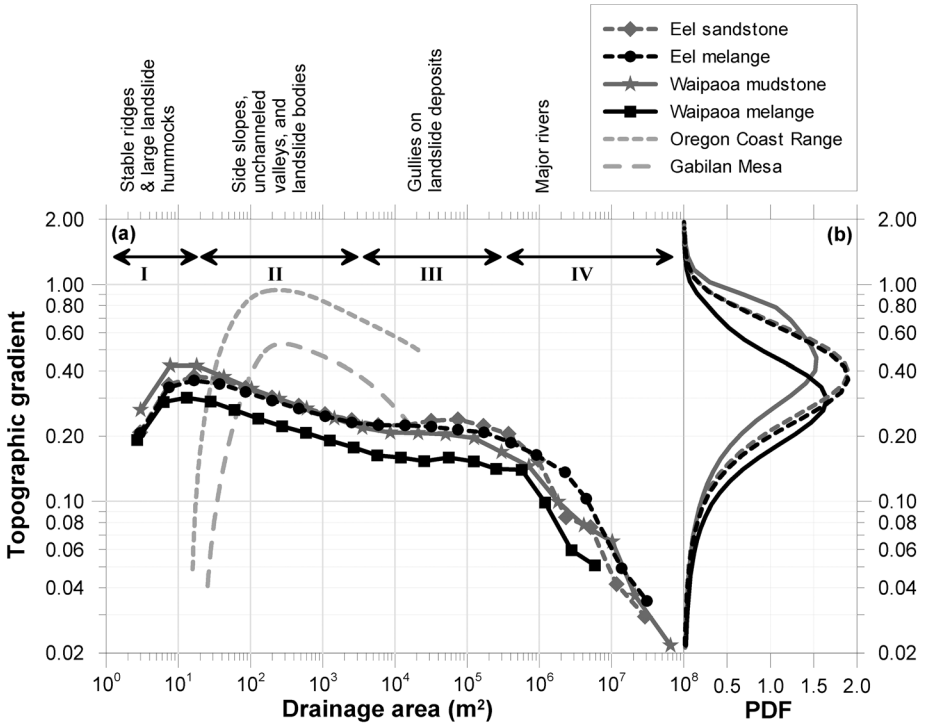

Figure 4. (a) Lidar-derived slope-area plots for the Waipaoa and Eel River study areas, subdivided by geologic unit (Figures 2 and 3), and the Oregon Coast Range and Gabilan Mesa for reference (reproduced from *Roering et al*. [2007] with permission). For the Eel and Waipaoa, the topographic gradient is the mean in each of 20 logarithmically spaced bins in drainage area, and standard errors are smaller than the symbols. Figure 5 illustrates the spatial arrangement of the four geomorphic process regimes indicated by roman numerals I–IV. (b) Probability density functions of lidar-derived topographic gradients.

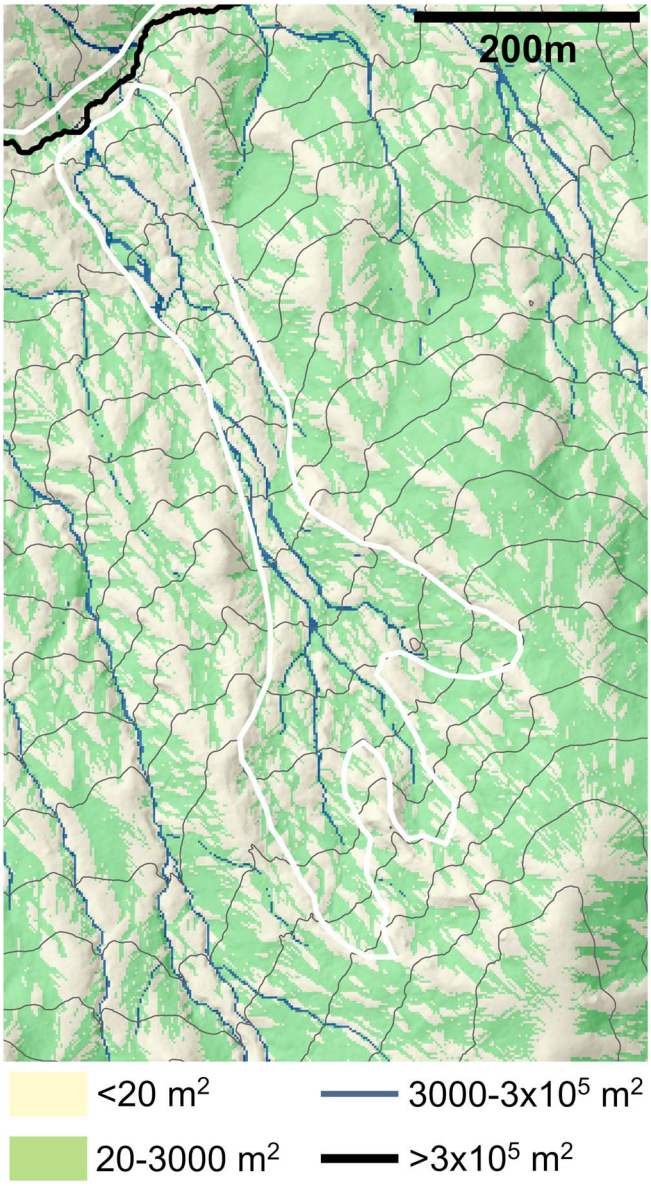

Figure 5. Lidar-derived hillshade map (Figure 3, white box), colored by drainage area, illustrating the spatial arrangement of the geomorphic process regimes identified in Figure 4. White outline delineates a historically active earthflow, and contour interval is 20 m.

terrain). This peak in the topographic gradient occurs at much lower drainage areas than for the soil-mantled, ridge-valley topography of the Oregon Coast Range and Gabilan Mesa, suggesting that deep-seated landslides affect the topography even at very small drainage areas near drainage divides. From drainage areas of ~20 m^2 to 3000 m^2, slope then monotonically decreases (regime II). In stable terrain, these grid cells delineate short side slopes adjacent to ridges and some unchanneled valleys, while in deep-seated landslide terrain, they are located just below scarps and in between hummocks throughout the landslide body (Figure 5, pale green terrain). At drainage areas of ~3000 m^2, topographic gradient tends to vary little or to slightly increase with increasing area up to ~3×10^5 m^2 (regime III). These data points correspond to small (meter-scale width and depth) channels, most of which are incised into the surfaces of active and relict deep-seated landslides (Figure 5, dark blue terrain). *Tarolli and Fontana* [2009] observed a similar process regime in a catchment with widespread landsliding, and we suggest that this pattern records the interplay between deep-seated landslides and channel processes such that landslide deformation inhibits the channels from attaining convex longitudinal profiles. Also, the Oregon Coast Range and Gabilan Mesa lack this process regime, instead transitioning directly from hillslopes to a well-established valley network at drainage areas of ~200 m^2. Finally, at drainage areas greater than ~3×10^5 m^2 (regime IV), slope decreases rapidly with increasing area, and these grid cells delineate the major, valley-forming channels that define the kilometer-scale ridge-valley topography described earlier (Figure 5, black line). The breadth of the distributions of topographic gradients (Figure 4b) reflects this diversity of processes regimes. Instead of a narrow distribution centered on a steep threshold slope, each of our study sites exhibits a wide range of slopes that result from interactions among deep-seated landslides and other geomorphic processes. Previous studies have shown that individual earthflows often have similar topographic gradients to the surrounding terrain suggesting that earthflows have shaped a large fraction of the surrounding landscape [*Mackey and Roering*, 2011; *Scheingross et al.*, 2013].

3. Landscape Evolution Model

3.1. Modeling Goals

[16] A landscape evolution model including deep-seated landsliding should be able to produce the most salient characteristics of deep-seated landslides in the context of landscape evolution. First, the model should produce the same topographic signatures identified in the preceding section, namely, the long, quasi-planar hillslopes and the process regimes in slope-area space (Figure 4). Additionally, landsliding is a stochastic process, where the rate and location of landsliding varies with time. Although this behavior is qualitatively replicated in mechanistic simulations with prescribed probabilities of slope failure [*Densmore et al.*, 1998, *Stark and Guzzetti*, 2009], we show that it can also emerge from a purely mechanistic model. Detailed mapping of slow-moving, deep-seated landslides reveals that most deep-seated landslides are actually landslide complexes, with many generations of landslides superimposed on one another [*Keefer and Johnson*, 1983; *Bovis*, 1985; *Mackey et al.*, 2009; *Mackey and Roering*, 2011] reflecting this stochastic nature. Our goal then is to develop a simple landscape evolution model that produces these general landslide characteristics and behaviors and is applicable to a wide range of deep-seated landslides in different geologic settings. We do so below based on observations of our study areas and by using mechanistic equations for deep-seated landsliding and other geomorphic processes.

3.2. Geomorphic Process Model

[17] Our landscape evolution model is based on conservation of mass, such that the change in the elevation of the land surface at any location in a landscape is the balance of fluxes into and out of that location [*Kirkby*, 1971; *Smith and*

Bretherton, 1972; *Ahnert*, 1976; *Willgoose et al*., 1991; *Howard*, 1994; *Tucker and Bras*, 1998]. In our study areas, we identify four key fluxes, each related to a specific geomorphic process: (1) uplift of bedrock relative to baselevel, (2) incision in channels, (3) near-surface soil creep, and (4) deep-seated landslide deformation of weathered material. For these four processes, continuity requires that

$$\frac{\partial z}{\partial t} = \frac{\rho_r}{\rho_{ls}} U - \varepsilon - \nabla\cdot(\boldsymbol{q}_s + \boldsymbol{q}_{ls}), \tag{1}$$

where z (with units of length, L) is the land surface elevation, t (T) is time, ρ_r ($M\ L^{-3}$) is the bulk density of bedrock, ρ_{ls} ($M\ L^{-3}$) is the bulk density of weathered material, U ($L\ T^{-1}$) is the vertical uplift rate relative to baselevel, ε ($L\ T^{-1}$) is the vertical rate of channel incision, $\boldsymbol{q}_s$ ($L^2\ T^{-1}$) is the horizontal soil creep flux per unit contour width, $\boldsymbol{q}_{ls}$ ($L^2\ T^{-1}$) is the horizontal deep-seated landslide flux per unit contour width, and boldface type indicates vectors. In this framework, each geomorphic process represented on the right-hand side of equation (1) acts everywhere in the landscape at all times, and the landscape's particular form results from a competition among these processes over time [*Smith and Bretherton*, 1972; *Howard*, 1994; *Tucker and Bras*, 1998]. We propose a new geomorphic transport law to determine the deep-seated landslide flux but rely on established geomorphic transport laws for the remaining geomorphic processes.

[18] The first term on the right-hand side of equation (1) is a source term, where U is the vertical bedrock uplift rate relative to baselevel, and the density ratio, ρ_r/ρ_{ls}, allows for a volumetric expansion as that rock is weathered and converted to mobile sediment. In our model, we assume uplift is spatially and temporally uniform relative to a fixed baselevel in order to isolate the effects of the surface processes in shaping the modeled drainage basin.

[19] The second term on the right-hand side of equation (1) describes the rate of incision due to overland flow of water. We use a general stream power type model [*Howard and Kerby*, 1983] to describe this process, which assumes that the incision rate is a power law function of drainage area and topographic gradient, such that

$$\varepsilon = KA^m|\nabla z|^n, \tag{2}$$

where K ($L^{1-2m}\ \mathrm{T}^{-1}$) is a coefficient of erosion, A (L^2) is drainage area, $|\nabla z|$ is the magnitude of the topographic gradient, and m and n are dimensionless constants. Equation (2) derives from the assumption that incision is detachment limited without a threshold such that all material eroded from the bed is transported completely out of the system. The drainage area, A, serves as a proxy for a characteristic water discharge, so that the exponent m reflects hydraulic geometry, drainage basin hydrology, and the dependence of incision on shear stress [*Whipple and Tucker*, 1999].

[20] The first flux term on the right-hand side of equation (1) describes the transport of near-surface sediment by soil creep, which results from the dilation and subsequent settling of soil particles due to a variety of biologic and physical processes [*Selby*, 1993]. This flux increases with the magnitude of the topographic gradient, resulting in convex hillslopes [*Gilbert*, 1877, 1909; *Davis*, 1892]. We assume a linear relationship for this dependence [*Culling*, 1960; *McKean et al*., 1993; *Small et al*., 1999], which is applicable to gently sloping, soil-mantled landscapes:

$$\boldsymbol{q}_s = -D\nabla z, \tag{3}$$

where D is a constant with the same units as a diffusivity ($L^2\ T^{-1}$). If hillslopes steepen beyond a gradient of ~0.6, a nonlinear dependence of flux on gradient is more appropriate, as shown by *Roering et al*. [1999] for the Oregon Coast Range, for example. However, most parts of our study, areas have gentler slopes (Figure 4b), and we focus on modeling landscapes with similarly gentle slopes.

[21] The final flux term in equation (1) describes the transport of material by deep-seated landslides, the expression for which we propose based on observations of landslides in our study areas and similar landslides elsewhere. In general, to predict landslide flux at any location in a landscape, one needs to determine the landslide's thickness and velocity at that location, which suggests an equation of the form

$$\boldsymbol{q}_{ls} = \bar{\boldsymbol{u}_{ls}} H, \tag{4}$$

where $\bar{\boldsymbol{u}_{ls}}$ ($L\ T^{-1}$) is the vertically averaged velocity and H (L) is the thickness [*Tucker and Hancock*, 2010]. Most slope failures in both our study areas are "composite earth slide-earth flows" [*Cruden and Varnes*, 1996], which transport sediment down slope through a combination of fluid-like internal deformation and frictional slip on a shear surface [*Brunsden*, 1984; *Keefer and Johnson*, 1983; *Zhang et al*., 1991; *Swanston et al*., 1995; *Baum et al*., 2004]. Vertical velocity profiles from borehole inclinometer data from these types of landslides therefore commonly have a plug flow shape in which a millimeter- to meter-scale shear zone at the base of the landslide accommodates most of the shear strain, while material near the surface translates essentially as a rigid block [*Keefer and Johnson*, 1983; *Iverson*, 1986a; *Pyles et al*., 1987; *Malet and Maquaire*, 2003]. Properties of this shear zone, modulated by fluid pressure in the pore spaces as the material deforms, control landslide motion over daily to seasonal timescales [*Iverson and Major*, 1987; *Hilley et al*., 2004; *Iverson*, 2005; *Schulz et al*., 2009a]. However, it remains unclear how landslide deformation evolves over longer timescales when multiple generations of landslide activity distributed throughout a catchment interact with other geomorphic processes to set the long-term topographic characteristics of that catchment. We therefore adopt a general, continuum mechanics approach that reproduces the general form of landslide velocity profiles in order to simulate landslide behavior. In doing so, we deliberately sacrifice some of the details of short timescale landslide motion in exchange for a landslide model that easily couples with other geomorphic transport laws in a grid-based numerical landscape evolution model. Specifically, we assume a non-Newtonian rheology [*Barnes et al*., 1989] for modeled landslides with the form

$$\dot{e}_{ij} = a\sigma_{\mathrm{eff}}^{p-1}\sigma_{ij}, \tag{5}$$

where e_{ij} (T^{-1}) is a component of the strain rate tensor, a ($L^p\ M^{-p}\ T^{2p-1}$) is a flow law constant, σ_{eff} ($M\ L^{-1}\ T^{-2}$) is the effective stress, p is a dimensionless flow law exponent, and σ_{ij} ($M\ L^{-1}\ T^{-2}$) is the corresponding component of the deviatoric stress tensor ($M\ L^{-1}\ T^{-2}$). *Iverson*

[1986a, 1986b, 1986c] used a similar rheology-based approach to investigate the response of an earthflow to perturbations to its stress field, while *Vulliet and Hutter* [1988a, 1988b, 1988c] and *Vulliet* [2000] have accurately predicted the deformation of slow-moving landslides over yearly time scales using this and similar rheologies in finite element models. To implement equation (5) in a longer-term landscape evolution model, we make a simplifying assumption that shear in the down slope direction is the dominant component of the deviatoric stress tensor, such that

$$\boldsymbol{\sigma} \approx \begin{pmatrix} 0 & 0 & \tau_{xz} \\ 0 & 0 & \tau_{yz} \\ \tau_{zx} & \tau_{zy} & 0 \end{pmatrix}, \tag{6}$$

where the subscripts refer to a slope-normal coordinate system. The effective stress then reduces to

$$\sigma_{\text{eff}} = \sqrt{\tau_{xz}^2 + \tau_{yz}^2}. \tag{7}$$

[22] Note that ice also deforms according to equation (5) with $p \sim 3$ [*Glen*, 1955], and glacier and ice sheet models commonly refer to the assumptions in equations (6) and (7) as the shallow ice approximation [*Hutter*, 1983]. Given this shallow flow approximation, the magnitudes of τ_{xz} and τ_{yz} are given by the x and y components of the shear stress vector, $\boldsymbol{\tau}$ ($M\,L^{-1}\,T^{-2}$), at depth, d (L), in a landslide, determined by

$$\boldsymbol{\tau} = \rho_{ls} g d \nabla z, \tag{8}$$

where g ($L\,T^{-2}$) is gravitational acceleration. Substituting equation (8) into equations (5) and (7) gives the shear strain rate as

$$\frac{\partial \boldsymbol{u}}{\partial z} = a(\rho g d)^p |\nabla z|^{p-1} \nabla z, \tag{9}$$

where $\boldsymbol{u}$ ($L\,T^{-1}$) is the horizontal velocity vector [*Rutt et al.*, 2009]. Integrating equation (9) once with respect to z gives the vertical velocity profile within the landslide:

$$\boldsymbol{u} = \frac{a(\rho_{ls} g)^p |\nabla z|^{p-1}}{p+1} \left(H^{p+1} - (H-h)^{p+1} \right) \nabla z, \tag{10}$$

where h (L) is height above the base of the landslide [*Huybrechts*, 1990; *Turcotte and Schubert*, 2002, p. 311]. The shape of this velocity profile depends nonlinearly on h, with different values of p controlling shear localization. For $p = 1$, the velocity profile is parabolic as for a Newtonian viscous fluid, while the profile becomes more plug-like with increasing p and approaches that of a rigid block with an infinitesimally small shear zone as $p \to \infty$. Integrating equation (10) with respect to z gives the depth-integrated landslide flux per unit contour width:

$$\boldsymbol{q}_{ls} = \frac{a(\rho_{ls} g)^p |\nabla z|^{p-1}}{p+2} H^{p+2} \nabla z, \tag{11}$$

which has the form of a geomorphic transport law and incorporates readily into the mass balance framework of equation (1).

[23] Importantly, equation (11) depends strongly on landslide thickness, which can vary substantially with time and location in a landslide-prone catchment. In order to predict landslide thickness in our model, we note that the deepest shear zones determined from borehole measurements in deep-seated earthflows are typically at or just above the interface between intact bedrock and weathered material [*Swanson and Swanston*, 1977; *Brunsden*, 1984; *Trotter*, 1993]. In our study areas, at several locations where deep channel incision has exposed shear zones, these zones also occur at or within a few centimeters of the interface between weathered material and fresh bedrock. This correspondence suggests that landslides in our study areas tend to initiate in the weaker weathered material just above fresh bedrock or that landslide shear zones tend to enhance weathering at that depth. We assume the former for the purposes of this model based on studies of groundwater-driven weathering of mudrocks similar to those in our study areas [*Rempe et al.*, 2010; *Salve et al.*, 2012; *Rempe and Dietrich*, 2012; *Dietrich et al.*, 2012]. In these lithologies, the groundwater table likely sets the maximum depth of weathering, which results in a high hydraulic conductivity contrast between fresh and weathered rock. This causes groundwater to become seasonally perched above the fresh bedrock, further enhancing weathering and generating high pore pressures in the weaker rock just above this interface. In this interpretation, deep-seated earthflows are not often thicker than the weathered zone because the strength of the underlying intact bedrock is much greater. Just above the fresh bedrock, high shear stresses and high seasonal pore water pressures in weak material make shear zones more likely to develop. At a broader spatial scale, *Gage and Black* [1979] noted that widespread deep-seated landsliding occurred near our Waipaoa study area in response to a dramatic lowering of the groundwater table and weathering front following the last glacial maximum. This suggests that shear zones tend to migrate downward through time, relative to the uplifting terrain, in approximate concordance with the weathering front.

[24] We incorporate this behavior into our model by tracking the weathering front and allowing all material above this interface to deform and contribute to the deep-seated landslide flux according to equation (11). The subsurface of the modeled landscape therefore consists of fresh rock, which is not allowed to deform, and weathered rock, which is allowed to deform. Mobile landslide material at any location in the landscape can come directly from bedrock weathering or from the transport of pre-existing weathered material. In a simpler one-dimensional model, *Booth and Roering* [2011] assumed a constant weathered zone thickness as a first-order approximation. Here, we instead follow previous landscape evolution models [*Ahnert*, 1976; *Densmore et al.*, 1998; *Hergarten and Neugebauer*, 1998, 1999] and let the production of weathered material from bedrock evolve with time according to

$$P = P_0 \exp\left(-H/H_o\right), \tag{12}$$

where P ($L\,T^{-1}$) is the weathering rate, P_0 ($L\,T^{-1}$) is the maximum weathering rate when the weathered thickness is zero, and H_0 (L) is a characteristic thickness. Equation (12) is commonly used to model soil production from saprolite with H_0 typically less than 1 m [e.g., *Heimsath et al.*, 1997], but in this study, we assume that a production function of this form holds for deep weathering of intact bedrock as well, with $H_0 > 1$. Several studies of the chemical

weathering of bedrock support this assumption [*Gabet et al.*, 2006; *Burke et al.*, 2007; *Lebedeva et al.*, 2007], but defining a production function for the deep weathering of fresh bedrock remains an active area of research.

[25] Substituting equations (2), (3), and (11) into equation (1) gives the governing equation for our landscape evolution model:

$$\frac{\partial z}{\partial t} = \frac{\rho_r}{\rho_{ls}} U - KA^m|\nabla z|^n + D\nabla^2 z - \frac{a(\rho_{ls} g)^p}{p+2}\nabla\cdot\left(|\nabla z|^{p-1} H^{p+2}\nabla z\right), \quad (13)$$

which describes the time evolution of the land surface elevation at every location in a drainage basin and is coupled to equation (12) to determine H (section A and equations (A1), (A2), and (A9)). We refer to the first term on the right-hand side of equation (13) as the source term since it describes the steady addition of mass to the modeled catchment by uplift relative to baselevel. We refer to the second term as the fluvial incision term, which describes a nonlinear advective process with an effective velocity of $KA^m|\nabla z|^{n-1}$. The third term is the soil creep term, which has a diffusive form and an effective diffusivity of D. We refer to the last term as the landslide term, which has the form of nonlinear diffusion with an effective diffusivity of $a(\rho_{ls}g)^p|\nabla z|^{p-1}H^{p+2}/(p+2)$.

3.3. Numerical Model

[26] To test whether our landscape evolution model captures the fundamental landslide behaviors outlined in section 3.1, we implement equations (12) and (13) in a numerical model that simulates the evolution of a ~ 1 km^2 catchment, which is similar in size to those in our study areas. We integrate equation (13) forward in time using finite differences (section A) until the time-averaged sediment flux leaving the model catchment balances the tectonic flux into the catchment and focus on these steady state model landscapes. The initial condition for the land surface elevation is a plane with meter-scale random roughness and a mean elevation of 2 m, while the initial condition for the elevation of the weathering front is also a plane with meter-scale roughness, but a mean elevation of 0 m. One corner of the modeled drainage basin is fixed at an elevation of 0 m, while the rest of the model domain uplifts relative to this baselevel. No flux boundary conditions on the remaining boundary nodes ensure that material uplifted into the model domain leaves the catchment through this fixed elevation outlet. To focus our modeling efforts, we use the same constant values for some of the free parameters in equation (13), such that $\rho_r = 2700$ kg m^{-3}, $\rho_{ls} = 1700$ kg m^{-3}, $m = 0.5$, and $n = 1$ in all our model runs. Regarding this value of m, note that the numerical scheme assumes a channel width in each node that is smaller than the grid spacing and scales as $A^{0.5}$ (section A and equations (A4)–(A5)). This effectively increases m and results in more concave channel longitudinal profiles than those produced when $m = 0.5$. We focus on a flow law exponent of $p = 3$, which is within the range of 1 to 15 reported in previous studies [*Vulliet and Hutter*, 1988a, 1988b, 1988c; *Vulliet*, 2000] and allows the model to run in a reasonable amount of time (section A), but briefly explore the effects of higher p values in section 4.4.

4. Results

[27] Using the numerical model described above, we fully explore the parameter space and characterize the tectonic and geomorphic conditions at which landslides occur in the modeled catchment. We first estimate the flow law constant, a (equations (5)–(11)), for a variety of deep-seated landslides throughout the world (Table 1). We then show that the model produces three distinct landscape types which can be classified within a parameter space defined by two non-dimensional numbers. The first type of landscape is unaffected by landsliding and consists of ridge-valley topography. The second is characterized by steady landsliding, in which the landslide flux accommodates a large fraction of the total flux, but remains constant through time at each location within the catchment. The third is dominated by stochastic landsliding, whereby discrete landslide events episodically transport material at rates exceeding the long-term rate of baselevel fall. The first non-dimensional number is the ratio of the characteristic landslide flux to the tectonic flux, and this number defines when the topography transitions from being dominated by soil creep and fluvial incision to being dominated by deep-seated landslides. The second non-dimensional number is the ratio of the modeled catchment's initial weathered zone thickness to the steady state weathered zone thickness, which characterizes the initial conditions that result in stochastic landsliding. We then examine catchment-scale topographic measures by tracking the influence of deep-seated landsliding on mean topographic gradients and valley spacing, and conclude by demonstrating that the model produces the same topographic signatures, recorded by slope-area statistics, as are found in our study areas.

4.1. Estimation of the Landslide Parameter *a*

[28] To determine what values of a to use in our numerical simulations, with the flow law exponent fixed at $p = 3$, we applied equation (10) to previously studied deep-seated landslides with observations of velocity, thickness, and topographic gradient from borehole data (Table 1) [*Keefer and Johnson*, 1983; *Vulliet and Hutter*, 1988a, 1988b; *Zhang et al.*, 1991; *Cristescu et al.*, 2002; *Malet and Maquaire*, 2003; *Borgatti et al.*, 2006; *Savage and Wasowski*, 2006]. For studies that reported a complete vertical velocity profile, we iteratively determined the value of a that minimized the root mean square error between the predicted and observed velocity profiles. If the study provided only a surface velocity, we set $h = H$ in equation (10) and solved for a directly. The best-fit values of a range from $\sim 10^{-63}$ m^3 kg^{-3} yr^5 for the slower and deeper landslides to $\sim 10^{-55}$ m^3 kg^{-3} yr^5 for the faster and thinner landslides, since a is proportional to u and inversely proportional to H^{p+1} (equation (10)). At a given study site, a often varies by an order of magnitude or more when determined from borehole data at different locations or at different times on the same landslide. This could be due to the material properties of the landslide actually changing from one location or time to another, or might be an artifact of using a shallow flow approximation, which ignores longitudinal stresses. Nonetheless, these order of magnitude estimates suggest the approximate range of a to explore in our numerical simulations described below. For several velocity profiles, a larger p resulted in a slightly better fit, but we focus on $p = 3$ for consistency among the many model runs

Table 1. Estimation of the Flow Law Constant, a

Reference	Reference Figure	Density, ρ_{ls} (kg m^{-3})	Depth, H (m)	Slope, $\lvert\nabla z\rvert$	Flow Law Constant, a (m^3 kg^{-3} yr^5)[a]
Borgatti et al. [2006]	Figure 8	2000	16	0.25[c]	10^{-61}
Cristescu et al. [2002]	Figure 12	1700[b]	20	0.29[d]	10^{-62}
	Figure 13	1700[b]	8	0.36[d]	10^{-61}
Keefer and Johnson [1983]	Figure 29	1730	0.5	0.27[e]	10^{-55}
Malet and Maquaire [2003]	Figure 3	1700[b]	9	0.46[e]	10^{-61}
Savage and Wasowski [2006]	Figure 8	1700[b]	17	0.12[d]	10^{-60}
Vulliet and Hutter [1988a]	Figure 1a	2041	26.5	0.23	10^{-63}
	Table 2	2041	20	0.16	10^{-62}
		2041	14.85	0.19	10^{-62}
		2041	22	0.07	10^{-62}
		2041	15.35	0.29	10^{-62}
Vulliet and Hutter [1988b]	Figure 8	1700[b]	7	0.27[e]	10^{-59}
Zhang et al. [1991]	Figure 4, G	1800	5	0.47	10^{-58}
	Figure 4, H	1800	5	0.09	10^{-56}
	Figure 4, M	1800	6	0.14	10^{-58}
	Figure 4, N	1800	3	0.32	10^{-57}

[a]From best-fit velocity profile when $p = 3$.
[b]Approximate density because not provided in reference.
[c]Approximate slope based on reported mobilized friction angle.
[d]Approximate slope based on reported topographic maps.
[e]Approximate slope based on reported average slope.

reported in the following sections, and briefly report the influence of higher values of p in section 4.4.

4.2. Non-Dimensionalization and Identification of Three Landscape Classes

[29] One measure of the importance of landslides in shaping a model catchment is the size the landslide term (the last term on the right-hand side of equation (13)) relative to the fluvial incision and soil creep terms (the second and third terms on the right-hand side of equation (13), respectively). To compare the sizes of these terms, we non-dimensionalize equation (13) with the aim of being able to estimate the characteristic length scales with analytical solutions to the governing equations when possible, or by measuring them directly from the modeled topography. We take ζ as a characteristic vertical length scale associated with uplift, ξ as a characteristic vertical length scale associated with weathering, λ as a characteristic horizontal length scale, and $\theta = \zeta/U$ as a characteristic time scale. By using length scales specific to each process included in the model, we ensure that the derivatives in the non-dimensional governing equation are of order unity for straightforward comparison of the magnitudes of each term. Substituting $z^* = z/\zeta$, $H^* = H/\xi$, $x^* = x/\lambda$, $y^* = y/\lambda$, and $t^* = t/\theta$ gives the non-dimensional governing equation as

$$\frac{\partial z^*}{\partial t^*} = \rho^* - K^* A^{*m} |\nabla z^*|^n + D^* \nabla^2 z^* - V^* \nabla \cdot \left(|\nabla z^*|^{p-1} H^{*p+2} \nabla z^* \right), \tag{14}$$

where

$$\rho^* = \frac{\rho_r}{\rho_{ls}}, \tag{15a}$$

$$K^* = \frac{K \lambda^{2m-n} \zeta^n}{U}, \tag{15b}$$

$$D^* = \frac{D\zeta}{U\lambda^2}, \tag{15c}$$

$$\text{and } V^* = \frac{a(\rho_{ls} g)^p \zeta^p \xi^{p+2}}{U(p+2)\lambda^{p+1}}, \tag{15d}$$

and the asterisks denote dimensionless quantities. For a given model run, the quantities ρ_r, ρ_{ls}, K, U, D, a, and p are specified directly, while the quantities λ, ζ, and ξ evolve with time according to equations (12) and (13). We therefore outline a straightforward approach for estimating these three length scales using either analytical solutions to the governing equations or measurements of the resulting topography. The steady state weathered zone thickness is a natural choice for ξ, which can be predicted for any model run by

$$\xi = -H_0 \ln\left(\frac{U}{P_0}\right). \tag{16}$$

[30] For the characteristic horizontal length scale, λ, we use the hillslope length scale, defined as one half of the first-order valley spacing. For modeled landscapes where landsliding is unimportant ($V^* = 0$), this can be estimated using

$$\lambda = \left(\frac{D}{K}\zeta^{1-n}\right)^{\frac{1}{2(m+1)-n}}, \tag{17}$$

assuming that the fluvial incision and soil creep terms are the only significant contributors to sediment transport in the catchment [*Perron et al.*, 2008a]. The steady state hillslope relief is a natural choice for ζ, but it is often quite variable across a landscape and not known a priori for a given model run. We therefore assume instead that the catchment's mean topographic gradient, $|\bar{\nabla} z|$, is equivalent to ζ/λ, since this can easily be measured from the modeled topography and is quite consistent among different model runs with the same parameters. Substituting equation (17) into equation (15d) then yields a single non-dimensional number that captures the importance of the landslide term relative to the fluvial incision and soil creep terms:

$$V^* = \frac{a\left(\rho_{ls} g |\bar{\nabla} z|\right)^p \xi^{p+2}}{U(p+2)} \left(\frac{K}{D\zeta^{1-n}}\right)^{\frac{1}{2(m+1)-n}}. \quad (18)$$

[31] Specifically, V^* is the ratio of the average landslide flux per unit width (equation (11)) to the vertical tectonic flux per unit width, $U\lambda$, on a hillslope with a horizontal length scale set by equation (17). For $m = 0.5$ and $n = 1$, as we use in this study, equation (18) simplifies to

$$V^* = \frac{a\left(\rho_{ls} g |\bar{\nabla} z|\right)^p \xi^{p+2}}{U(p+2)} \left(\frac{K}{D}\right)^{\frac{1}{2}}, \quad (19)$$

which highlights the relative importance of each parameter on the right-hand side in determining V^* for a model catchment. All else being equal, V^* increases linearly with a and nonlinearly with ρ_{ls}, g, $|\nabla z|$, and ξ because each of these variables directly influences the magnitude of the deep-seated landslide flux (equation (11)). An increase in K or a decrease in D causes a weak nonlinear increase in V^* by decreasing the hillslope length scale, which increases the mean topographic gradient and therefore indirectly increases the landslide flux. An increase in U causes a decrease in V^* because it increases the vertical flux of material relative to the horizontal landslide flux.

[32] The non-dimensional landslide number, V^*, captures the overall importance of the landslide term in shaping topography but does not take into account the model's initial conditions. Landslide thickness is directly set by the weathered zone thickness in our model, and we find that the initial value of the weathered zone thickness plays an important role in determining whether or not the model produces stochastic landsliding. We define the normalized initial weathered zone thickness as

$$\xi^* = {}^{\xi_0}/_{\xi}, \quad (20)$$

where ξ_0 is the maximum initial weathered zone thickness of a model run.

[33] The non-dimensional landslide number, V^*, and the normalized initial weathered zone thickness, ξ^*, define a parameter space that classifies the three types of landscapes produced by the model: no landsliding, steady landsliding, and stochastic landsliding (Figure 6). In generating this example parameter space, we held $U = 1$ mm yr^{-1}, $D = 0.01$ m^2 yr^{-1}, and $K = 0.01$ yr^{-1} constant and ran the model over values of ξ ranging from ~0.8 to 8 m and values of a ranging from 10^{-64} to 10^{-58} m^3 kg^{-3} yr^5, as suggested by Table 1. These values correspond to $\xi^* \sim 0.4$ to 4 and $V^* \sim 10^{-3}$ to 10^3.

[34] On the left-hand side of this parameter space, we define the "no landsliding" regime as all landscapes with mean topographic gradients and standard deviations of weathered zone thicknesses that vary by less than 5% from those of landscapes where $V^* = 0$. In this regime, V^* is always less than ~2, and no landslides occur, indicating that the landslide term is unimportant relative to the soil creep and fluvial incision terms in shaping the topography. Landscapes in this regime consist of ridges and valleys, such as those in Figures 6d, 7c, 8c, and 9b, and the combination of soil creep on hillslopes and fluvial incision in channels alone keeps pace with tectonic uplift.

[35] In the lower right portion of the parameter space, we define the "steady landsliding" regime as all landscapes with a mean topographic gradient that is less than that of landscapes

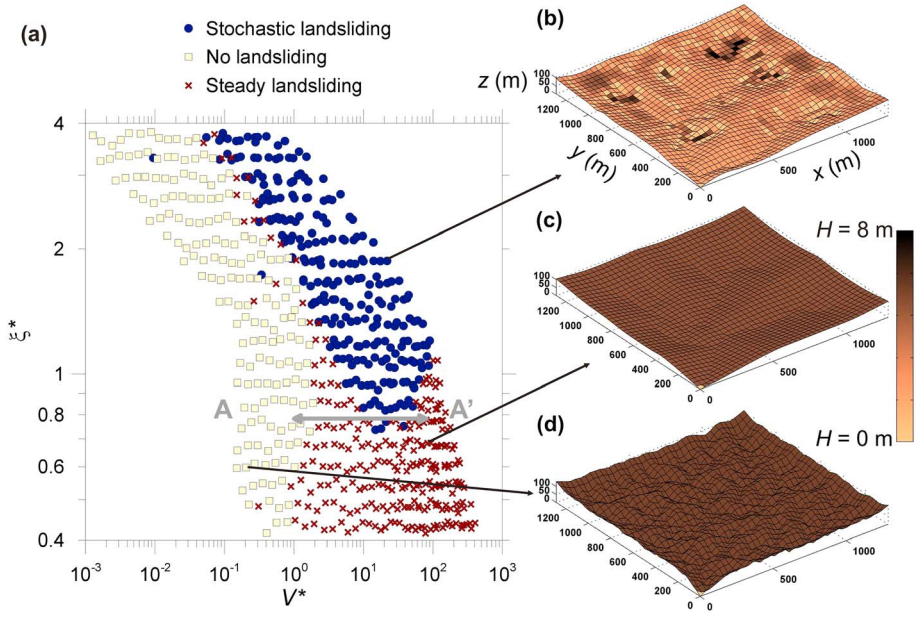

Figure 6. (a) Parameter space illustrating the three model landscape classes as a function of the non-dimensional landslide number, V^*, and the normalized initial weathered zone thickness, ξ^*. (b)–(d) Example landscapes of stochastic landsliding, steady landsliding, and no landsliding. Thin black arrows indicate the location of each example landscape in the parameter space, and shading is the weathered zone depth, H (m). Transect A-A′ in Figure 6a indicates the range of landscapes investigated in section 4.3.3 and shown in Figure 9.

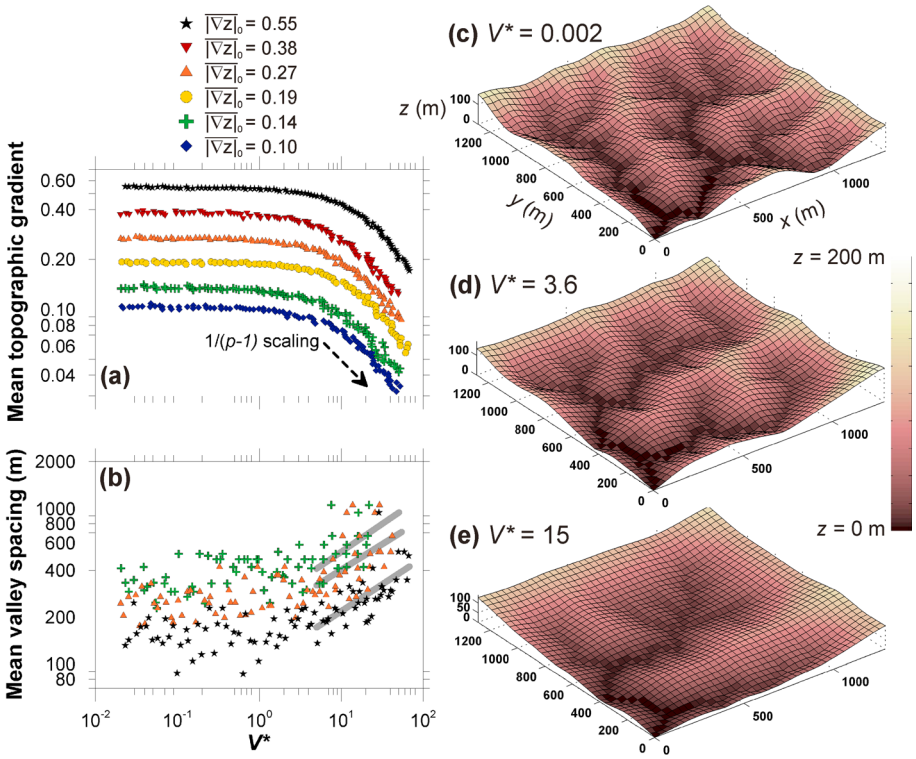

Figure 7. Dependence of (a) mean topographic gradient and (b) mean valley spacing of modeled catchments on V^* for small normalized initial weathered zone thicknesses. Table 2 gives the parameters used for each of the six model runs. For clarity, only three of the runs are shown in Figure 7b, and the gray lines are statistically significant fits for the data with $V^* > 5$, which highlight the increase in valley spacing with V^* in the landslide-dominated regime. (c)–(e) Examples of steady state landscapes resulting from small, moderate, and large values of V^*, respectively, from run #5 (▼ symbols). Shading is elevation, z (m).

where $V^* = 0$ by at least 5% but a standard deviation of weathered zone thicknesses that does not differ from that of landscapes where $V^* = 0$ by more than 5%. In this regime, V^* is greater than ~2, indicating that the landslide flux is large relative to uplift at the length scale set by the fluvial incision and soil creep terms. These landscapes have long, low angle, quasi-planar hillslopes, such as those in Figures 6c and 7e, because of the large, temporally steady, but spatially variable landslide flux. However, no discrete landslides occur, and instead, the flux of material out of each location in the model catchment exactly balances the sum of the vertical tectonic flux and the horizontal flux of material from upslope into that location at all times. The landslide term contributes a temporally constant proportion of the total flux at each location, but its relative contribution varies spatially. Because the weathered zone thickness, which sets landslide thickness, attains its constant steady state value under these model conditions, the topographic gradient alone controls the landslide flux throughout the catchment. Landslide fluxes are therefore highest and much larger than the soil creep and fluvial incision fluxes in valley heads and midway up valley side slopes where topographic gradients are highest and the topography transitions from being convex to concave.

[36] In the upper right portion of the parameter space, we define the "stochastic landsliding" regime as all landscapes with topographic gradients and standard deviations of weathered zone thicknesses that both differ from landscapes with $V^* = 0$ by more than 5%. Discrete landslide events occur in this regime, and the landslide flux varies dramatically in both time and space, even when the landscape is at a temporally averaged steady state. Individual landslide events tend to initiate in valley heads where topographic gradients are highest and then run out and deposit weathered material in the low order channel network. This episodic flux erodes weathered material locally at rates exceeding the steady tectonic uplift rate and prevents the weathered zone from attaining its predicted steady state value throughout the model catchment (Figures 6b, 8d, 3e, and 9c).

[37] This regime requires a relatively large ξ^*, confirming the important control initial conditions have on the behavior of the modeled landscape. When the weathered zone is initially very deep, a thick mantle of weathered material already covers much of the landscape as it steepens from the nearly flat initial surface. Upstream propagation of knickpoints as the fluvial network becomes established then rapidly steepens areas underlain by this thick weathered zone, triggering discrete landslide events. A positive feedback between the topographic gradient and the landslide flux therefore initiates stochastic landsliding only when there is a thick mantle of weathered material already in place. A landslide triggered in this way typically reactivates several times at the same location until it reduces the topographic gradient to a value where the landslide flux once again approximately balances the sum of the flux from upslope and the local tectonic flux. These landslides' deposits are also thick compared to the steady state weathered zone thickness and have low topographic gradients,

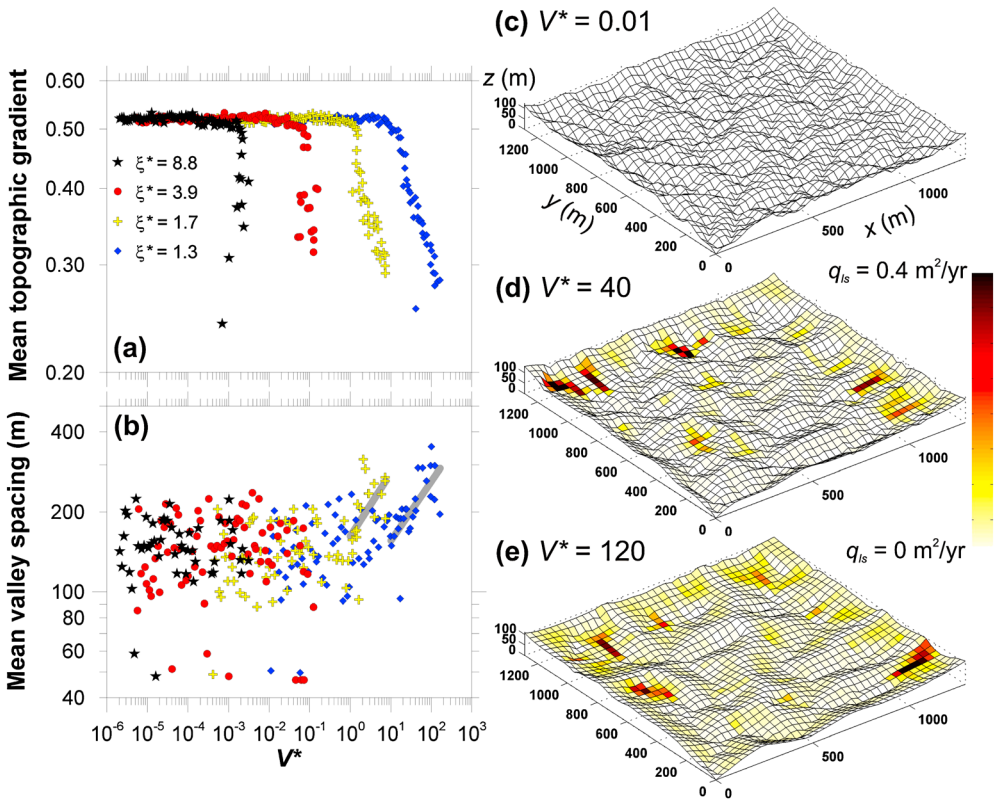

Figure 8. Dependence of (a) mean topographic gradient and (b) mean valley spacing of modeled catchments on V^* for large normalized initial weathered zone thicknesses and stochastic landsliding. Table 3 gives the parameters used for each of the four model runs. Gray lines in Figure 8b are statistically significant fits for the data with $V^* > 10$ and $V^* > 1$ for runs 1 and 2, respectively. (c)–(e) Examples of steady state landscapes resulting from small, moderate, and large values of V^*, respectively, from run #1 (blue ♦ symbols). Shading is landslide flux (per unit width), q_{ls} (m^2 yr^{-1}).

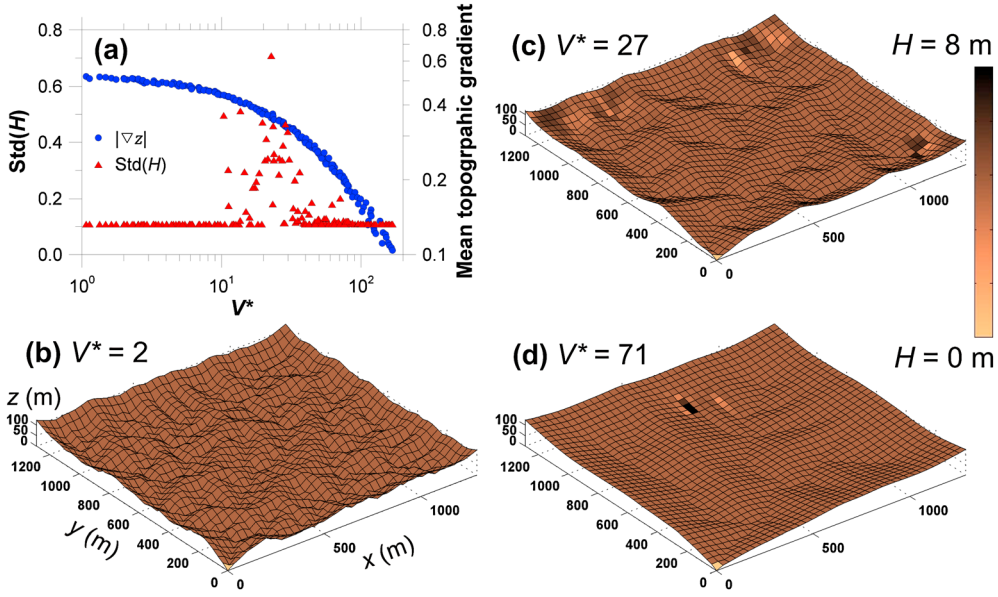

Figure 9. (a) Dependence of the mean topographic gradient and standard deviation of weathered zone depths on V^* along transect A-A′ in Figure 6. (b)–(d) Examples of steady state landscapes for small, moderate, and large values of V^*, colored by weathered zone thickness, H (m).

so they persist as the landscape uplifts, and can be rapidly incised again at a later time, repeating the cycle. Each subsequent episode of landsliding therefore typically initiates at a different location than the previous, wherever incipient channels rapidly incise landslide deposits. This cyclic behavior implies that model landscapes in the stochastic landsliding regime rarely transition out of this regime, and we did not observe such a transition in any of the model runs described in this study. Similar positive feedbacks involving non-Newtonian flow laws have been observed in ice sheet models [*Fowler and Johnson*, 1996; *Payne and Dongelmans*, 1997; *Hindmarsh*, 2009], but the specific mechanism differs. In ice, the flow law constant, a, is temperature dependent such that increasing temperature increases the flux, while in our landslide flow law, a is constant and increasing the topographic gradient increases the flux.

4.3. Mean Topographic Gradient and Valley Spacing

[38] To connect these three types of landscapes to more general, catchment-scale topographic metrics, we track the mean topographic gradient and valley spacing produced by models over a range of V^* for several different normalized initial weathered zone thicknesses. We first examine thin initial weathered zones where the landscape transitions from no landsliding to steady landsliding with increasing V^*. We then investigate thick initial weathered zones where the landscape transitions from no landsliding to stochastic landsliding. Last, we explore moderate initial weathered zones, which can result in all three landscape types.

4.3.1. Thin Initial Weathered Zones

[39] For thin initial weathered zones ($\xi^* < 0.85$), we ran a series of models as described in section 3.3 with six different combinations of parameters on the right-hand side of equation (19) and tracked the mean topographic gradient and mean valley spacing of the resulting steady state topography (Table 2 and Figure 7). We first determined unique combinations of U, D, and K that produced landscapes with mean topographic gradients ranging from ~0.1 to 0.5 with the landslide term set to zero. We then ran the model 100 times, each time with a different value of a, suggested by our estimates in section 4.1, in order to span a wide range of V^* that included the transition from soil creep and fluvial incision dominated landscapes to deep-seated landslide dominated landscapes. We determined mean valley spacing by first estimating the power spectrum of the steady state topography using the two-dimensional discrete Fourier transform [*Perron et al.*, 2008b]. We then normalized the power spectrum by a red noise spectrum with a lag-1 autocorrelation of $\alpha = 0.7$ [*Gilman et al.*, 1963; *Torrence and Compo*, 1997], which gave the best fit to the majority of the model-generated power spectra. Last, we defined the wavelength at the peak of this normalized spectrum as the characteristic valley spacing.

[40] For each of these model landscapes, the landslide term affects neither the mean topographic gradient (Figure 7a) nor the mean valley spacing (Figure 7b) when V^* is less than ~2, and these landscapes (Figure 7c) are statistically indistinguishable from landscapes where $V^* = 0$. At $V^* \sim 2$, the mean topographic gradient begins to decrease with V^*, the mean valley spacing begins to increase, and hillslopes become more planar in both profile and plan form (Figure 7d). Topographic gradient and valley spacing continue their trajectories with additional increases in V^*, and when V^* is greater than ~5, the low gradient, quasi-planar hillslopes begin to approach the scale of the modeled catchment (Figure 7e). We refer to this critical value of V^* as V^*_{crit} since it marks the transition from landscapes dominated by soil creep and fluvial incision to landscapes dominated by deep-seated landsliding. In this regime, the mean topographic gradient tends to decrease as $V^{*-1/(p-1)}$ (Figure 7a), as predicted by equation (14) with $K^* = 0$ and $D^* = 0$. Mean valley spacing increases as $V^{*0.36\pm0.32}$, $V^{*0.33\pm0.26}$, and $V^{*0.35\pm0.13}$ ($V^{*\text{mean} \pm 95\% \text{ confidence interval}}$) for model runs 2, 4, and 6, respectively (Figure 7b).

4.3.2. Thick Initial Weathered Zones

[41] To determine how thick normalized initial weathered zones affect the nature of the transition from soil creep and fluvial incision dominated landscapes to deep-seated landslide dominated landscapes, we ran another series of models with different maximum weathering rates (equation (12)), which gave thin steady state weathered zone thicknesses and therefore large normalized initial weathered zone thicknesses (Table 3). For this series of model runs, we kept $U = 1$ mm yr^{-1}, $D = 0.01$ m^2 yr^{-1}, and $K = 0.01$ yr^{-1} constant, and then ran the model 100 times over a range of a values and determined the mean topographic gradient and valley spacing as described at the end of section 4.3.1.

[42] For each of these modeled landscapes, the mean topographic gradient is unaffected when $V^* < V^*_{crit}$ (Figures 8a and 8c). However, unlike the gradual transition to the steady flux landslide dominated regime reported in section 4.3.1, the onset of landsliding in these model runs is abrupt and marked by a dramatic decrease in mean topographic gradient when $V^* > V^*_{crit}$ (Figures 8a, 8d, and 8e). In model runs 1 and 2, mean valley spacing increases with

Table 3. Parameters Used to Generate Figure 9[a]

Run #	P_0 (m yr^{-1})	ξ (m)	ξ^*	a Range (m^3 kg^{-3} yr^5)	Symbol
1	2.0×10^{-3}	2.8	1.25	10^{-65}–10^{-59}	♦
2	1.7×10^{-3}	2.1	1.67	10^{-67}–10^{-61}	+
3	1.3×10^{-3}	0.9	3.89	10^{-64}–10^{-58}	●
4	1.1×10^{-3}	0.4	8.75	10^{-66}–10^{-60}	⋆

[a] $U = 1$ mm yr^{-1}, $D = 0.01$ m^2 yr^{-1}, and $K = 0.01$ yr^{-1} held constant.

Table 2. Parameters Used to Generate Figure 8

Run #	U (m yr^{-1})	D (m^2 yr^{-1})	K (yr^{-1})	P_0 (m yr^{-1})	H_0 (m)	ξ^*	a range (m^3 kg^{-3} yr^5)	Symbol
1	1.0×10^{-5}	4.0×10^{-3}	3.0×10^{-4}	2.0×10^{-5}	8	0.63	10^{-65}–10^{-59}	♦
2	1.0×10^{-5}	4.0×10^{-3}	2.0×10^{-4}	2.0×10^{-5}	16	0.32	10^{-67}–10^{-61}	+
3	1.0×10^{-4}	1.0×10^{-2}	3.0×10^{-3}	2.0×10^{-4}	12	0.42	10^{-64}–10^{-58}	●
4	1.0×10^{-4}	1.0×10^{-2}	1.3×10^{-3}	2.0×10^{-4}	8	0.63	10^{-66}–10^{-60}	▲
5	1.0×10^{-4}	1.0×10^{-2}	7.0×10^{-4}	2.0×10^{-4}	16	0.32	10^{-67}–10^{-61}	▼
6	1.0×10^{-3}	1.0×10^{-2}	7.0×10^{-3}	4.0×10^{-3}	16	0.16	10^{-68}–10^{-62}	⋆

V^* when $V^* > V^*_{crit}$, but mean valley spacing is insensitive to V^* over the range investigated for model runs 3 and 4 (Figure 7b and Table 3). To qualitatively explain this difference, we note that where landslides deposit material, the fluvial network must incise at this long-term deposition rate in addition to the background uplift rate for the landscape to maintain a temporally averaged steady state. When steady state weathered zones are relatively thin (runs 3 and 4), landslides are generally small with thin deposits, and the deposition rate is therefore small compared to the background uplift rate. In this scenario, the fluvial incision term can keep pace with both uplift and landslide deposition without major adjustments in channel slope or reconfiguration of the drainage network. However, when steady state weathered zones are thick (runs 1 and 2), landslide deposits are also thick, and the rate of deposition is large compared to the background uplift rate. In this case, the drainage network tends to steepen and reconfigure itself in order to acquire more drainage area above the locations of landslide deposits in order for incision to keep pace with the more rapid landslide deposition in addition to uplift. This combination of increasing drainage area above landslide deposits, increasing landslide size, and increasing long-term landslide deposition rate effectively widens valley spacing.

4.3.3. Moderate Initial Weathered Zones

[43] For moderate normalized initial weathered zone thicknesses ($\xi^* \sim 0.8$), which can produce all three landscape classes, we characterized landscapes along transect A-A′ in Figure 6 (Figure 9). In these model runs, we maintained a predicted steady state weathered zone thickness (equation (16)) of $\xi = 4.4$ m ($P_0 = 0.003$ and $H_0 = 4$), and varied a from 10^{-62} to 10^{-58} m^3 kg^{-3} yr^5. Other parameters were $U = 1$ mm yr^{-1}, $K = 0.01$ yr^{-1}, and $D = 0.01$ m^2 yr^{-1}.

[44] Similar to the case of steady landsliding, the mean topographic gradient begins to decrease at $V^* \sim 2$ and rolls over to decrease more rapidly after $V^*_{crit} \sim 5$ (Figure 9a). However, tracking the standard deviation of the weathered zone thicknesses highlights how the landscape transitions through the stochastic landsliding regime only when $V^* \sim 10$ to 70. For V^* less then ~ 10, the standard deviation of weathered zone thicknesses remains low and consistent among model runs as the landscape transitions from the no landsliding to the steady landsliding regime. However, at $V^* \sim 10$ a large fraction of model runs generate stochastic landsliding, marked by the approximately fivefold increase in the maximum standard deviation of weathered zone thicknesses. Stochastic landsliding directly causes this increase in variability by perturbing the weathered zone to shallower depths at landslide initiation sites and thickening the weathered zone in depositional areas (Figure 9c). This effect is strongest when V^* is just greater than V^*_{crit}, and the variability of weathered zone thickness tends to decrease with further increases of V^*. By $V^* \sim 50$, most model runs do not produce any stochastic landsliding, and those that do have only modestly elevated standard deviations of weathered zone thickness, marking a gradual transition to the steady landsliding regime once V^* exceeds ~ 70 (Figure 9d).

4.4. Effects of the Flow Law Exponent

[45] All model runs discussed above used a flow law exponent of $p = 3$, but the velocity profiles of many deep-seated landslides observed in nature are better fit with higher values. We therefore briefly explore the effects of higher flow law exponents on landscapes in the stochastic landsliding regime. To isolate the effects of p, we first take run #2 from Table 3 with $a = 2.4 \times 10^{-60}$ m^3 kg^{-3} yr^5 as a reference model, which falls in the stochastic landsliding regime at $V^* \sim 3.6$ and $\xi^* \sim 1.6$, and run the model with these parameters 50 times to determine the mean topographic gradient and standard deviation of weathered zone thicknesses produced by this combination of parameters. We then run two additional series of 50 model runs each, one with $p = 5$ and $a = 2.46 \times 10^{-98}$ m^5 kg^{-5} yr^9, and the other with $p = 7$ and $a = 2.27 \times 10^{-136}$ m^7 kg^{-7} yr^{13}, since these combinations of a and p give approximately the same landslide flux (equation (11)) for the mean thickness and topographic gradient of the reference case. For $p = 3$, 5, and 7, the mean topographic gradients of the modeled landscapes are 0.34 ± 0.03, 0.30 ± 0.04, and 0.29 ± 0.03 (mean ± 95% confidence interval), and the standard deviations of weathered zone thicknesses are 2.10 ± 0.78, 2.09 ± 1.28, and 2.08 ± 1.51 m. This indicates that landscapes shaped by landslides with different flow law exponents, but similar fluxes for a given topographic gradient and thickness, are morphologically similar and cannot be statistically distinguished based on their topographic attributes alone.

[46] Although the value of the flow law exponent does not affect the shape of the modeled landscapes, all else being equal, it does dramatically influence the maximum magnitude of the episodic fluxes of sediment from stochastic landslides (Figure 10). To illustrate, we track the mean landslide flux at each timestep of model runs with $p = 3$, 5, and 7 over ~ 700 ky. For $p = 3$, the maximum mean landslide flux is ~ 1 m^2 yr^{-1}, and it increases to $\sim 10^3$ m^2 yr^{-1} when $p = 5$ and to $\sim 10^5$ m^2 yr^{-1} when $p = 7$. This reflects the transition to landslides that behave more like threshold hillslopes as the landslide flux becomes increasingly nonlinear. For higher values of the flow law exponent, the landslide flux is increasingly sensitive to H or $|\nabla z|$ so that minor changes in either of these quantities can cause dramatic increases in the landslide flux. However, these more than order of

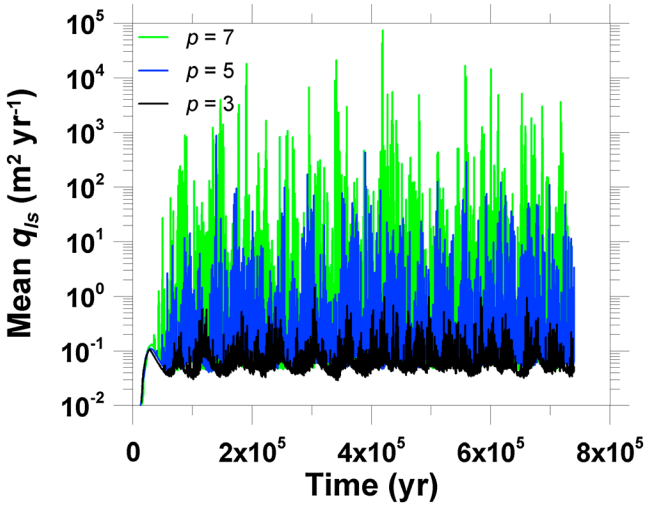

Figure 10. Mean landslide flux (per unit width) versus time for ~ 700 ky model runs with $p = 3$, 5, and 7 as described in section 4.4.

magnitude changes in the maximum landslide flux only slightly increase the time-averaged landslide flux over the ~700 ky model run from 0.05 m^2 yr^{-1} for $p=3$ to 0.07 and 0.08 m^2 yr^{-1} for $p=5$ and 7, respectively.

4.5. Topographic Signatures

[47] The topography associated with each of the three landscape types is recorded by the dependence of topographic gradient on drainage area (Figure 11). In generating Figure 11, we averaged the slope-area plots from all model landscapes in the no landsliding regime shown in Figure 6 and all landscapes with mean topographic gradients between 0.2 and 0.3 for the steady and stochastic landsliding regimes. In the no landsliding regime, the landscape consists of stable ridges and valleys and is dissected by the channel network down to the model's grid resolution in this example. Because of this, slopes are steepest at the smallest drainage areas and then decrease as a power law function of drainage area with a slope of −1 for areas greater than ~3×10^3 m^2, consistent with our model for fluvial incision (equation (2)). This power law slope differs from −0.5, as predicted by our choice of $m=0.5$ (section 3.3), because our numerical scheme assumes a channel width function that depends on drainage area (equation (A4)). In the steady landsliding regime, the topographic gradient first increases gradually up to a drainage area of ~10^4 m^2. This reflects the large landslide flux, relative to soil creep and fluvial incision, which predicts that for a constant landslide thickness, the magnitude of the topographic gradient should slightly increase nonlinearly with distance from a divide (equation (11)). For areas greater than ~10^4 m^2, slope decreases rapidly as a power law in agreement with equation (2). In the stochastic landsliding regime, the topographic gradient decreases steadily to a drainage area of ~10^5 m^2 and then decreases more rapidly in agreement with the fluvial incision model. This documents how stochastic landsliding in the model removes weathered material from the parts of the catchment with the lowest drainage areas and the steepest slopes and then deposits this material in the valley network, locally steepening low order channels (Figures 6b, 8d, and 8e). In both landsliding regimes, the slope is less than that of the no landsliding regime at low drainage areas but greater at high drainage areas because the landslide term contributes to net deposition in these concave areas of the landscape, forcing them to be steeper in order for fluvial incision to keep up with the uplift rate.

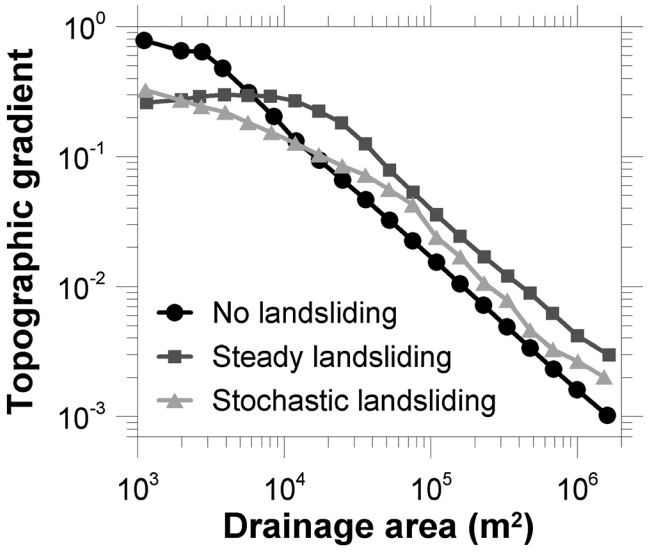

Figure 11. Representative slope-area plots from the no landsliding, steady landsliding, and stochastic landsliding regimes, averaged in 20 evenly spaced logarithmic bins. All modeled landscapes in the no landsliding regime from Figure 6 were used to determine the representative plot for no landsliding, while only landscapes with mean topographic gradients between 0.2 and 0.3 were used to determine the representative plots for both the steady and stochastic landsliding regimes.

[48] The slope-area plots from the stochastic and steady landsliding regimes both exhibit some characteristics of those documented in our study areas (Figure 4). The model's coarser spatial resolution does not resolve the initial peak in topographic gradient at ~20 m^2 evident in the lidar-derived slope-area plots but does capture the transition from the landslide-dominated lower drainage areas to the fluvial incision dominated higher drainage areas. In the steady landsliding regime, the slight increase of topographic gradient with drainage area, followed by the more rapid power law decline is similar to scaling regimes III and IV observed in our study areas. However, the stochastic landsliding regime lacks this increase in slope with drainage area, and instead appears to transition directly from regime II to regime IV. Both steady and stochastic landsliding push the transition to the fluvial incision dominated part of the slope-area plot to higher drainage areas, but stochastic landsliding pushes this transition point to larger drainage areas than steady landsliding. Although neither steady nor stochastic landsliding in the model produces all the characteristics of the lidar-derived slope-area plots, both types of landscapes capture the general trends of reduced topographic gradients near drainage divides, where landslides erode material, and steepened topographic gradients in the channel network, where landslides deposit material. This pushes the transition to the fluvial incision dominated part of the landscape to higher drainage areas.

4.6. Uplift Rate and Catchment Relief

[49] To put our landscape evolution model in a broader spatial and temporal context, we determined how topographic relief varies with uplift rate in each of the three landscape types produced by the model (Figure 12). To construct each relief-uplift rate curve we let $D=0.01$ m^2 yr^{-1}, $K=0.01$ yr^{-1}, $H_0=4$ m, $a=1\times10^{-60}$ m^3 kg^{-3} yr^5, and $U=0.05$ to 5 mm yr^{-1} and recorded the maximum elevation of each steady state modeled catchment. For the steady landsliding regime we let $P_0\sim7U$ in order to have a thin normalized initial weathered zone of $\xi^*\sim0.4$ and a steady state weathered zone thickness of ~8 m, for the stochastic landsliding regime we let $P_0\sim2U$ to give $\xi^*\sim1.2$ and $\xi\sim3$ m, and for the no landsliding regime we let $a=0$.

[50] In the no landsliding regime and for this combination of parameters, relief increases with uplift rate as $U^{0.99\pm0.03}$, ($U^{\text{mean}\ \pm\ 95\%\ \text{confidence interval}}$) which is consistent with equation (2) when $n=1$ [*Whipple and Tucker*, 1999] and predicted by equation (14) with $D^*=0$ and $V^*=0$ (Figure 12). The extent and steepness of the fluvial network therefore generates the majority of the total catchment relief with hillslopes above first-order valleys contributing only a small fraction of total relief. Catchments in the steady

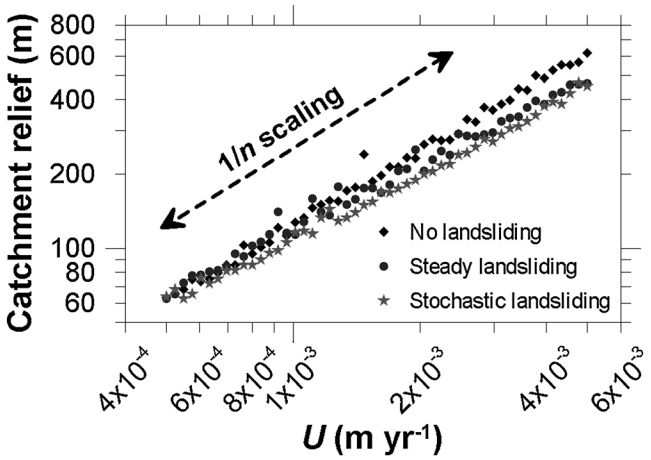

Figure 12. Relief versus uplift rate curves for modeled landscapes in each of the three landsliding regimes. In the no landsliding regime, relief scales as $U^{0.99\pm0.03}$ which is consistent with the fluvial incision model with $n=1$; in the steady landsliding regime, relief scales as $U^{0.91\pm0.02}$; and in the stochastic landsliding regime, relief scales as $U^{0.85\pm0.03}$. Landsliding therefore weakly but statistically significantly weakens the dependence of total catchment relief on uplift rate.

landsliding regime generally have less total relief for a given uplift rate, and relief scales as $U^{0.91\pm0.02}$, while catchments in the stochastic landsliding regime have even less relief for a given U, and relief scales as $U^{0.85\pm0.03}$. Both these relief-uplift scaling exponents are statistically significantly lower than that of the no landsliding regime, indicating that the presence of landsliding, especially stochastic landsliding, in the model slightly weakens the dependence of catchment relief on uplift rate. If landsliding were the only important process in the model ($D^*=0$ and $K^*=0$ in equation (14)), catchment relief would be the same as the local hillslope relief and would scale as $U^{1/p}$ [*Booth and Roering*, 2011]. However, the fact that the scaling exponents in both landsliding regimes are fairly close to unity indicates that the fluvial network still plays an important role in setting overall catchment relief, so long as the fluvial incision term is large enough to dissect the model catchment into ridges and valleys.

5. Discussion and Conclusions

[51] Our landscape evolution model captured the most salient characteristics of our study areas and should be adaptable to a wide variety of other landscapes. To apply the model to a given study area, one needs to independently estimate as many of the parameters in equations (11) and (13) as possible, some of which are more challenging to infer than others. For the landslide term, borehole deformation data, as we exploited here, is one way to estimate the key landslide parameters a and p. Since the model is meant to simulate long-term (longer than $\sim 10^3$ yr) landscape evolution, such measurements should record deformation over at least a season of movement in order for a and p to be representative of their average, long-term values. Also, for the shallow flow approximation to be most valid, deformation data should come from parts of a landslide with a constant topographic gradient and thickness, where longitudinal stresses are minimal. A combination of remote sensing and geophysical data could also potentially constrain the flow law parameters. For example, high-resolution topographic data (lidar) and repeat aerial photographs or satellite interferometry could provide spatially extensive information about topographic gradient and surface deformation [*Hilley et al*., 2004; *Strozzi et al*., 2005; *Schwab et al*., 2008; *Roering et al*., 2009; *Mackey and Roering*, 2011; *Delong et al*., 2012], while shallow geophysics such as shallow seismic, ground penetrating radar, or electrical resistivity could provide spatially extensive thickness information [*Jongmans and Garambois*, 2007; *Travelletti and Malet*, 2012].

[52] The model also provides a framework to predict how deep-seated landslide prone landscapes might respond to changes in climatic forcing. Changes in precipitation could affect the landslide flux by changing landslide average velocity or landslide thickness (equation (4)). Regarding velocity, many slow-moving landslides move seasonally once the groundwater table has risen sufficiently to raise pore water pressures and decrease the effective normal stresses [*Iverson and Major*, 1987]. After the onset of motion during the wet season, velocity often correlates with precipitation [*Keefer and Johnson*, 1983], and these wet season velocities are typically large and relatively constant compared to the much slower dry season velocities [*Iverson and Major*, 1987; *Zhang et al*., 1993; *Coe et al*., 2003; *Schulz et al*., 2009b]. This suggests that slow-moving landslides respond to longer wet seasons by moving slightly faster and for a longer period of time compared to dry years. The parameter a, which is based empirically on a landslide's deformation over a given time scale, is sensitive to this behavior if the time scale is longer than seasonal, with a proportionately larger value of a resulting from a longer period of landslide movement in a given season. Regarding landslide thickness, changes in the amount and duration of precipitation might affect H in the model by speeding up or slowing down weathering. In clay-rich lithologies such as those in our study areas, cyclic wetting and drying often drives weathering so that the weathering front tends to track the position of the lowest groundwater table [*Ollier*, 1969; *Franklin and Chandra*, 1972; *Matsukura and Mizuno*, 1986; *Stephenson and Kirk*, 2000; *Rempe et al*., 2010; *Rempe and Dietrich*, 2012]. Since this sets landslide thickness in our model, deeper weathering, perhaps due to a temporary period of decreased precipitation, would increase landslide flux once precipitation increased again. In the context of our Waipaoa study area, the rapid incision beginning ~18 k. a. [*Berryman et al*., 2000] lowered river channel elevations and groundwater levels, resulting in deeper weathering and perhaps a dramatic increase in deep-seated landsliding [*Gage and Black*, 1979].

[53] If a landscape is near a border between the regimes of Figure 6, such climatic changes might cause dramatic shifts in landslide behavior. We first consider a change in the duration of the wet season, which affects the parameter a as described above. For a landscape in the no landsliding regime, an increase in a would shift the landscape to the right on Figure 6, possibly causing an abrupt transition to stochastic landsliding if the weathering zone is thick relative to its steady state value, or a gradual transition to steady landsliding if the weathering zone is thin relative to its steady state value. For landscapes near the center of Figure 6, an increase in a could possibly push the landscape from the steady landsliding

regime to the stochastic landsliding regime, or further to the right, from the stochastic landsliding regime to the steady landsliding regime. A change in the position of the groundwater table, due to a change in the magnitude of precipitation seasonality, would affect landslide thickness as described in the preceding paragraph. An increase in thickness would shift a landscape up and strongly to the right on Figure 6 more dramatically than an increase in a since V^* increases nonlinearly as ξ^{p+2}. This implies that a slight increase in weathered zone thickness could push a landscape from the no landsliding regime to either of the landsliding regimes depending on the weathered zone thickness. Although we focused on $p = 3$ in this study, higher values of p relevant to landslides with very thin shear zones would increase the sensitivity of V^* to ξ, which we expect would cause such transitions to be even more abrupt.

[54] In conclusion, we proposed a general, mechanistic geomorphic transport law for slow-moving, deep-seated landslides and implemented this law in a landscape evolution model to determine the geomorphic conditions at which landsliding is important in shaping topography. The model generated three classes of landscapes—those with no landsliding, steady landsliding, and stochastic landsliding. We derived a non-dimensional landslide number, defined as the ratio of the characteristic horizontal landslide flux to the vertical tectonic flux, which characterized each of these landscape types in combination with the model's initial conditions. If the initial weathered zone thickness, which set landslide thickness, was small relative to its steady state value, landscapes transitioned gradually from the no landsliding regime to the steady landsliding regime with increases in the non-dimensional landslide number. In this steady landsliding regime, the large landslide flux systematically reduced mean topographic gradients and widened valley spacing, but this flux remained constant in both time and space once the model attained a topographic steady state. If the initial weathered zone was thick relative to its steady state value, landscapes transitioned abruptly from the no landsliding to the stochastic landsliding regime at a critical value of the non-dimensional landslide number. In this stochastic landsliding regime, discrete landslides episodically transported material at rates exceeding the long-term average erosion rate, and the locations of these landslides varied through time. Reduced topographic gradients, wider valley spacing, and highly variable weathered zone thicknesses characterized this landscape regime. When the initial weathered zone thickness was the same order as the steady state thickness, the landscape transitioned through all three landscape types with increases in the non-dimensional landslide number. Both the stochastic and steady landsliding regimes produced slope-area plots with some of the same characteristics as those of our two study areas. Landsliding reduced topographic gradients at low drainage areas where landslides initiated in the model, increased topographic gradients in the low order channel network where landslides deposited material, and thereby pushed the transition to the fluvial incision dominated parts of the landscape to higher drainage areas. We suggest that this is the first landscape evolution model to accurately capture the most salient features of slow-moving, deep-seated landslides in the context of landscape evolution, and that our proposed geomorphic transport law for these landslides is adaptable to a wide range of geologic settings.

Appendix A: Numerical Solution of Equations (12) and (13)

[55] We solved the coupled equations (12) and (13) by tracking the time evolution of the bedrock elevation, b, and the land surface elevation, z, on a finite difference grid. For each time step of duration Δt, we determined b using the explicit scheme

$$b_{i,j}^{k+1} = b_{i,j}^{k} + \Delta t \left[U - P_0 \exp\left(\frac{-\left(z_{i,j}^{k} - b_{i,j}^{k}\right)}{H_0} \right) \right], \tag{A1}$$

where the subscripted i and j refer to indices of locations within the model domain, and the superscripted k indexes the time step. We determined z using the explicit scheme

$$z_{i,j}^{k+1} = z_{i,j}^{k} + \Delta t \left(\frac{\partial z}{\partial t} \right)^{k}. \tag{A2}$$

[56] To approximate $\partial z/\partial t$ at time step k, we used finite difference approximations of the derivatives in each of the terms on the right-hand side of equation (13). For the fluvial incision term, we used an upwind scheme, which defines the topographic gradient as the forward difference in the direction of steepest descent [*Pelletier*, 2008, p. 93], such that

$$|\nabla z|_{i,j} = \left| \frac{\Delta z}{\delta x} \right|_{D8}, \tag{A3}$$

where Δz is the change in elevation over a horizontal distance of δx and the subscripted D8 indicates the direction of steepest descent between a node and its eight nearest neighbors [*O'Callaghan and Mark*, 1984]. If the steepest descent is in the x or y direction, $\delta x = \Delta x$ and $\Delta z = z_{i\pm1,j} - z_{i,j}$ or $z_{i,j\pm1} - z_{i,j}$, while on the diagonal, $\delta x = \sqrt{2\Delta x^2}$ and $\Delta z = z_{i\pm1,j\pm1} - z_{i,j}$, assuming a grid spacing of Δx in both the x and y directions. We also calculated the drainage area using the D8 algorithm. To minimize potential grid size effects arising from the fluvial incision model, we assumed that all channels in the model catchment have a width, w, that is smaller than the grid size and given by the empirical relationship

$$w_{i,j} = 0.005\sqrt{A_{i,j}}. \tag{A4}$$

[57] During each time step, the numerical scheme determined the volume of erosion in a channel of width w and length Δx and then distributed this amount of erosion evenly over the entire grid cell [*Howard*, 1994; *Perron et al.*, 2008a; *Carretier et al.*, 2009]. Substituting equation (A4) into the fluvial incision model (equation (2)) subject to these assumptions gives the fluvial incision rate in a grid cell as

$$\varepsilon_{i,j} = \frac{0.005 K A_{i,j}^{m+0.5} |\nabla z|_{i,j}^{n}}{\Delta x}, \tag{A5}$$

which has an additional factor of $A^{0.5}$ compared to equation (2). For $m = 0.5$ as used in this study, this technique therefore generates highly concave channel longitudinal profiles such that $|\nabla z| \propto A^{-1}$ at large drainage areas rather than a more commonly observed scaling of $|\nabla z| \propto A^{-0.5}$ (Figure 11). The upwind scheme (equation (A3)) introduces numerical diffusion [S*molarkiewicz*, 1983] with an effective diffusivity, D_{num}, that varies spatially in the case of the fluvial incision model and depends on the size of the time step:

$$D_{\mathrm{num}\,i,j} = \frac{Kw_{i,j}A_{i,j}^{m}|\nabla z|_{i,j}^{n-1}}{2}\left(1 - \frac{\Delta t K w_{i,j}A_{i,j}^{m}|\nabla z|_{i,j}^{n-1}}{\Delta x^2}\right). \quad \text{(A6)}$$

[58] We eliminated this effect by applying the *Smolarkiewicz* [1983] correction

$$\Delta\tilde{z}_{i,j} = -\Delta t\left|\frac{\Delta(D_{\mathrm{num}}|\nabla z|)}{\delta x}\right|_{D8}, \quad \text{(A7)}$$

where $\Delta\tilde{z}_{i,j}$ indicates a small correction to be made to $z_{i,j}^{k+1}$ each time step. For the soil creep term, we discretized the Laplacian operator using a five-point stencil:

$$\nabla^2 z = \frac{z_{i+1,j} + z_{i-1,j} + z_{i,j+1} + z_{i,j-1} - 4z_{i,j}}{\Delta x^2}. \quad \text{(A8)}$$

[59] The landslide term has the form of a nonlinear diffusion equation, which generally requires the use of staggered grids for conditional stability in a finite difference model. We implemented this technique following *Oerlemans and van der Veen* [1984] by first calculating the effective nonlinear diffusivity as

$$D_{\mathrm{eff}\,i,j} = \frac{a(\rho_{ls}g)^p\left(\left(\frac{z_{i+1,j}-z_{i-1,j}}{2\Delta x}\right)^2 + \left(\frac{z_{i,j+1}-z_{i,j-1}}{2\Delta x}\right)^2\right)^{\frac{p-1}{2}}H_{i,j}^{p+2}}{p+2}, \quad \text{(A9)}$$

where $H_{i,j} = z_{i,j} - b_{i,j}$, at each node in the regular finite difference grid. We then calculated the flux on a staggered grid consisting of points halfway between each of the nodes in the regular finite difference grid in the x and y directions. For example, the flux at the point on the staggered grid halfway between the node at (i,j) and $(i+1,j)$ is

$$q_{ls\,i+1/2,j} = \frac{D_{\mathrm{eff}\ i+1,j} + D_{\mathrm{eff}\ i,j}}{2}\frac{z_{i+1,j} - z_{i,j}}{\Delta x}, \quad \text{(A10)}$$

which is in the x direction. Using equivalent expressions for the flux at the three remaining neighboring nodes in the staggered grid, the divergence of the landslide flux at node (i,j) is

$$(\nabla\cdot q_{ls})_{i,j} = \frac{q_{ls\,i+1/2,j} - q_{ls\,i-1/2,j} + q_{ls\,i,j+1/2} - q_{ls\,i,j-1/2}}{\Delta x}. \quad \text{(A11)}$$

[60] The above finite difference scheme implies different maximum stable time steps for the fluvial incision, soil creep, and landslide terms given by

$$\Delta t \le \frac{\Delta x}{\left(KwA^m|\nabla z|^{n-1}\right)_{\max}}, \quad \text{(A12)}$$

$$\Delta t \le \frac{\Delta x^2}{2D}, \quad \text{(A13)}$$

$$\text{and } \Delta t \le \frac{\Delta x^2}{4(D_{\mathrm{eff}})_{\max}}, \quad \text{(A14)}$$

respectively, where the subscripted *max* indicates the maximum value of the quantity in parentheses within the model domain. We used an adaptable time step equal to the minimum of equations (A12)–(A14), which for most simulated landscapes was set either by the fluvial incision term at the node with the greatest drainage area or by the landslide term where the quantity $|\nabla z|^{p-1}H^{p+2}$ was greatest.

Appendix B: Time Step Resolution Tests

[61] To confirm that our identification of the stochastic landsliding regime was not an artifact of the time step chosen for the numerical solution, we ran a series of models with maximum time steps of $\Delta t_{\max}$, $0.1\Delta t_{\max}$, and $0.01\Delta t_{\max}$, using the same parameter values as in Run #2 of section 4.3.2 (Table 3 and Figure 8). Over this two order of magnitude range in time steps, the scaling of the mean topographic gradient and the scaling of the standard deviation of weathered zone thicknesses with the non-dimensional landslide number are indistinguishable, and the abrupt transition from the no landsliding to the stochastic landsliding regime occurs at the same value of $V^* \sim 1.5$ (Figure B1a). Additionally, we recorded a time series of the mean landslide flux (per unit width) for three simulations with the different time steps and $a = 2.44 \times 10^{-60}$ m^3 kg^{-3} yr^5 (Figure B1b). Although the timing of individual landslides in each time series is different, the means and standard deviations of the flux for each time series are statistically indistinguishable with $q_{ls} = 0.05 \pm 0.02$ m^2 yr^{-1} (mean $\pm$ standard deviation) when $\Delta t = \Delta t_{\max}$, $q_{ls} = 0.07 \pm 0.04$ m^2 yr^{-1} when $\Delta t = 0.1\Delta t_{\max}$, and $q_{ls} = 0.06 \pm 0.03$ m^2 yr^{-1} when $\Delta t = 0.01\Delta t_{\max}$. These lines of evidence suggest that the stochastic landsliding regime is not a numerical artifact and instead results from feedbacks in the governing equations between landsliding and weathering given certain initial conditions (section 4.2).

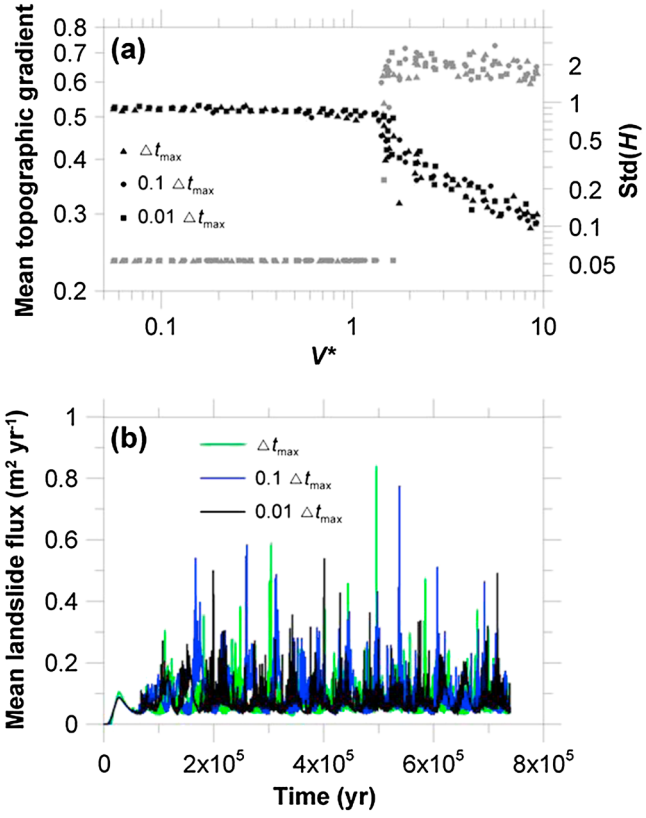

Figure B1. (a) Mean topographic gradient (black symbols) and standard deviation of weathered zone thicknesses (gray symbols) versus V^* and (b) mean landslide flux (per unit width) versus time for models run with time steps of $\Delta t_{\max}$, $0.1\Delta t_{\max}$, and $0.01\Delta t_{\max}$ and all other parameters equal.

[62] **Acknowledgments.** This work was supported by a NSF Graduate Research Fellowship to AMB, and NSF OCE-0841111 and NASA NNX08AF95G awards to JJR. Greg Tucker, Paolo Tarolli, and Junko Iwahashi provided thorough reviews, and the associate editor Simon Mudd provided additional comments that helped clarify the results and improve the quality of the manuscript. AMB thanks J. Taylor Perron for many landscape evolution modeling discussions and comments on preliminary results; Ben Mackey, Alex Handwerger, Corina Cerovski-Darriau, and Eric Bilderback for many landslide discussions; and Jill Marshall, Rob Skarbek, and Kristin Sweeney for numerous discussions of landscape evolution.

References

Ahnert, F. (1976), Brief description of a comprehensive three-dimensional process-response model of landform development, *Z. Geomorphol. Suppl.*, *25*, 29–49.

Ahnert, F. (1977), Some comments on the quantitative formulation of geomorphological processes in a theoretical model, *Earth Surf. Processes*, *2*, 191–202.

Bak, P., C. Tang, and K. Wiesenfeld (1988), Self-organized criticality, *Phys. Rev. A*, *38*, 364–374.

Barnes, H. A., J. F. Hutton, and K. Walters (1989), *An Introduction to Rheology*, pp. 15–25, Elsevier, Amsterdam.

Baum, R. L., W. Savage, and J. Wasowski (2004), Mechanics of earth-flows, in Proceedings of the International Workshop on Occurrence and Mechanisms of Flow-Like Landslides in Natural Slopes and Earthfills, edited by L. Picarelli, pp.185–190, Patron Ed., Bologna, Italy.

Berryman, K., M. Marden, D. Eden, C. Mazengarb, Y. Ota, and I. Moriya (2000), Tectonic and paleoclimatic significance of Quaternary river terraces of the Waipaoa River, East Coast, North Island, New Zealand, *N. Z. J. Geol. Geophys.*, *43*, 229–245.

Booth, A. M., and J. J. Roering (2011), A 1-D mechanistic model for the evolution of earthflow-prone hillslopes, *J. Geophys. Res.*, *116*, F04021, doi:10.1029/2011JF002024.

Borgatti, L., A. Corsini, M. Barbieri, G. Sartini, G. Truffelli, G. Caputo, and C. Puglisi (2006), Large reactivated landslides in weak rock masses: A case study from the Northern Apennines (Italy), *Landslides*, *3*, 115–124, doi:10.1007/s10346-005-0033-9.

Bovis, M. J. (1985), Earthflows in the Interior Plateau, southwest British Columbia, *Can. Geotech. J.*, *22*, 313–334.

Brunsden, D. (1984), Mudslides, in Slope Instability, edited by D. Brunsden and D. B. Prior, pp. 363–418, John Wiley & Sons Ltd., Chichester, UK.

Burbank, D. W., J. Leland, E. Fielding, R. S. Anderson, N. Brozovic, M. R. Reid, and C. Duncan (1996), Bedrock incision, rock uplift and threshold hillslopes in the northwestern Himalayas, *Nature*, *379*, 505–510, doi:10.1038/379505a0.

Burke, B. C., A. M. Heimsath, and A. F. White (2007), Coupling chemical weathering with soil production across soil-mantled landscapes, *Earth Surf. Process. Landforms*, *32*, 853–873, doi:10.1002/esp.1443.

Blodgett, T. A., and B. L. Isacks (2007), Landslide erosion rate in the Eastern Cordillera of Northern Bolivia, *Earth Interactions*, *11*, 1–30, doi:10.1175/2007EI222.1.

Carretier, S., B. Poisson, R. Vassallo, E. Pepin, and M. Farias (2009), Tectonic interpretation of transient stage erosion rates at different spatial scales in an uplifting block, *J. Geophys. Res.*, *114*, F02003, doi:10.1029/2008JF001080.

Coe, J. A., W. L. Ellis, J. W. Godt, W. Z. Savage, J. E. Savage, J. A. Michael, J. D. Kibler, P. S. Powers, D. J. Lidke, and S. Debray (2003), Seasonal movement of the Slumgullion landslide determined from Global Positioning System surveys and field instrumentation, July 1998–March 2002, *Eng. Geol.*, *68*, 67–101, doi:10.1016/S0013-7952(02)00199-0.

Cristescu, N. D., O. Cazacu, and C. Cristescu (2002), A model for slow motion of natural slopes, *Can. Geotech. J.*, *39*, 924–937, doi:10.1139/T02-040.

Crosby, B. T., and K. X. Whipple (2006), Knickpoint initiation and distribution within fluvial networks: 236 waterfalls in the Waipaoa River, North Island, New Zealand, *Geomorphology*, *82*, 16–38, doi:10.1016/j.geomorph.2005.08.023.

Cruden, D. M., and D. J. Varnes (1996), Landslide types and processes, in Landslides Investigation and Mitigation, edited by A. K. Turner and R. L. Schuster, pp. 36–75, National Academy Press, Washington, D.C.

Culling, W. E. H. (1960), Analytical theory of erosion, *Geology*, *68*, 336–344, doi:10.1086/626663.

Dadson, S. J., and M. Church (2005), Postglacial topographic evolution of glaciated valleys: a stochastic landscape evolution model, *Earth Surf. Processes*, *30*, 1387–1403, doi:10.1002/esp.1199.

Davis, W. M. (1892), The convex profile of bad-land divides, *Science*, *20*, 245.

DeLong, S. B., C. S. Prentice, G. E. Hilley, and Y. Ebert (2012), Multitemporal ALSM change detection, sediment delivery, and process mapping at an active earthflow, *Earth Surf. Processes*, *37*, 262–272, doi:10.1002/esp.2234.

Densmore, A. L., M. A. Ellis, and R. S. Anderson (1998), Landsliding and the evolution of normal-fault-bounded mountains, *J. Geophys. Res.*, *103*, B7, 15203–15219.

Dietrich, W. E., D. G. Bellugi, L. S. Sklar, J. D. Stock, A. M. Heimsath, and J. J. Roering (2003), Geomorphic transport laws for predicting landscape form and dynamics, in Prediction in Geomorphology, Geophys. Monogr. Ser, vol. *135*, edited by P. R. Wilcock and R. M. Iverson, pp. 103–132, AGU, Washington, D. C.

Dietrich, W. E., D. M. Rempe, and J. Oshun (2012), The influence of the deep critical zone under hillslopes on hydrologic, geomorphic and ecological processes, Abstract EP41I-08 presented at the 2012 Fall Meeting, AGU, San Francisco, Calif., 3–7 Dec.

Eyles, G. O. (1985), The New Zealand Land Resource Inventory Erosion Classification, Water and Soil Miscellaneous Publication no. 85, Ministry of Works and Development, Soil Conservation Centre, Aokautere, Ministry of Works, Palmerston North, New Zealand.

Fowler, A. C., and C. Johnson (1996), Ice sheet surging and ice stream formation, *Ann. Glaciol.*, *23*, 68–73.

Franklin, J. A., and R. Chandra (1972), The slake-durability test, *Intl. J. Rock Mech. Min. Sci.*, *9*, 325–341.

Furlong, K. P., and R. Govers (1999), Ephemeral crustal thickening at a triple junction: The Mendocino crustal conveyor, *Geology*, *27*, 127–130, doi:10.1130/0091-7613(1999)027<0127:ECTAAT>2.3.CO;2.

Furlong, K. P., and S. Y. Schwartz (2004), Influence of the Mendocino triple junction on the tectonics of coastal California, *Annu. Rev. Earth Planet. Sci.*, *32*, 403–433, doi:10.1146/annurev.earth.32.101802.120252.

Gabet, E. J., B. A. Pratt-Sitaula, and D. W. Burbank (2004), Climatic controls on hillslope angle and relief in the Himalayas, *Geology*, *32*, 629–632, doi:10.1130/G20641.1.

Gabet, E. J., R. Edelman, and H. Langner (2006), Hydrological controls on chemical weathering rates at the soil-bedrock interface, *Geology*, *34*, 1065–1068, doi:10.1130/G23085A.1.

Gage, M., and R. D. Black (1979), Slope-stability and geological investigations at Mangatu State Forest, *N. Z. For. Serv., Tech. Pap. 66*, 37 pp., N.Z. For. Serv., Wellington, New Zealand.

Gilbert, G. K. (1877), Geology of the Henry Mountains, U.S. Geographical and Geological Survey of the Rocky Mountains Region, Washington D.C.

Gilbert, G. K. (1909), The convexity of hilltops, *J. Geol.*, *17*, 344–350.

Gilman, D. L., F. J. Fuglister, and J. M. Mitchell, Jr. (1963), On the power spectrum of "red noise", *J. Atmos. Sci.*, *20*, 182–184.

Glen, J. W. (1955), The creep of polycrystalline ice, *P. Roy. Soc. Lond. A Mat.*, *228*, 519–538.

Gomez, B., and D. M. Livingston (2012), The river it goes right on: Post-glacial landscape evolution in the upper Waipaoa River basin, eastern North Island, New Zealand, *Geomorphology*, *159*, 73–83, doi:10.1016/j.geomorph.2012.03.006.

Griffiths, G. A. (1982), Spatial and temporal variability in suspended sediment yields of North Island basins, New Zealand, *J. Am. Water Resour. As.*, *18*, 575–584, doi:10.1111/j.1752-1688.1982.tb00038.x.

Heimsath, A. M., W. E. Dietrich, K. Nishiizumi, and R. C. Finkel (1997), The soil production function and landscape equilibrium, *Nature*, *388*, 358–361.

Hergarten, S., and H. J. Neugebauer (1998), Self-organized criticality in a landslide model, *Geophys. Res. Lett.*, *25*, 801–804.

Hergarten, S., and H. J. Neugebauer (1999), Self-organized criticality in landsliding processes, in Process Modelling and Landform Evolution, Lecture Notes in Earth Sciences, vol. *78*, edited by S. Hergarten and H. J. Neugebauer, pp. 231–249, Springer, Berlin/Heidelberg/New York.

Hilley, G. E., R. Bürgmann, A. Ferretti, F. Novali, and F. Rocca (2004), Dynamics of slow-moving landslides from permanent scatterer analysis, *Science*, *304*, 1952–1955, doi:10.1126/science.1098821.

Hindmarsh, R. C. A. (2009), Consistent generation of ice-streams via thermo-viscous instabilities modulated by membrane stresses, *Geophys. Res. Lett.*, *36*, L06502, doi:10.1029/2008GL036877.

Hovius, N., C. P. Stark, and P. A. Allen (1997), Sediment flux from a mountain belt derived by landslide mapping, *Geology*, *25*, 231–234, doi:10.1130/009-7613(1997)025 < 0231:SFFAMB > 2.3.CO;2.

Hovius, N., P. Meunier, L. Dhing-Weei, C. Hongey, C. Yue-Gau, S. Dadson, H. Ming-Hame, and M. Lines (2011), Prolonges seismically induced erosion and the mass balance of a large earthquake, *Earth Planet. Sc. Lett.*, *304*, 347–355, doi:10.1016/j.epsl.2011.02.005.

Howard, A. D. (1994), A detachment-limited model of drainage basin evolution, *Water Resour. Res.*, *30*, 2261–2285.

Howard, A. D., and G. Kerby (1983), Channel changes in badlands, *Geol. Soc. Am. Bulletin*, *94*, 739–752.

Hutter, K. (1983), *Theoretical Glaciology: Material Science of Ice and the Mechanics of Glaciers and Ice Sheets*, pp. 256–332, D. Reidel Publishing Co., Dordrecht.

Huybrechts, P. (1990), A 3-D model for the Antarctic ice sheet: A sensitivity study on the glacial-interglacial contrast, *Climate Dynamics*, *5*, 79–92.

Iverson, R. M. (1986a), Dynamics of slow landslides: A theory for time-dependent behavior, in Hillslope Processes, edited by A. D. Abrahams, pp. 297–317, Allen and Unwin, Winchester, MA.

Iverson, R. M. (1986b), Unsteady, nonuniform landslide motion: 1. Theoretical dynamics and the steady datum state, *J. Geol.*, *94*, 1–15.

Iverson, R. M. (1986c), Unsteady, nonuniform landslide motion: 2. Linearized theory and the kinematics of transient response, *J. Geol.*, *94*, 349–364.

Iverson, R. M. (2005), Regulation of landslide motion by dilatancy and pore pressure feedback, *J. Geophys. Res.*, *110*, F02015, doi:10.1029/2004JF000268.

Iverson, R. M., and J. J. Major (1987), Rainfall, groundwater flow, and seasonal movement at Minor Creek landslide, northwestern California: Physical interpretation of empirical relations, *Geol. Soc. Am. Bull.*, *99*, 579–594.

Jessen, M. R., T. F. Crippen, M. J. Page, W. C. Rijkse, G. R. Harmsworth, and M. McLeod (1999), Land use capability classification of the Gisborne-East Coast region, Landcare Research Science Series 21, pp. 1–213, Manaaki Whenua Press, Lincoln, New Zealand.

Jongmans, D., and S. Garambois (2007), Geophysical investigation of landslides: A review, *Bulletin Société Géologique de France*, *178*, 1–24, doi:10.2113/gssgfbull.178.2.101.

Keefer, D. K., and A. M. Johnson (1983), Earthflows: Morphology, mobilization and movement, *U.S. Geologic Survey Professional Paper 1256*, United States Government Printing Office, Washington, D.C.

Kelsey, H. M. (1978), Earthflows in Franciscan mélange, Van Duzen river basin, California, *Geology*, *6*, 361–364, doi:10.1130/0091-7613(1978)6<361:EIFMVD>2.0.CO;2.

Kirkby, M. J. (1971), Hillslope process-response models based on the continuity equation, *Spec. Publ. Inst. Br. Geogr.*, *3*, 15–30.

Kirkby, M. J. (1987), General models of long-term slope evolution through mass movement, in Slope Stability: Geotechnical Engineering and Geomorphology, edited by M. G. Anderson and K. S. Richards, pp. 359–379, Wiley and Sons, Chichester, U.K.

Korup, O. (2008), Rock type leaves topographic signature in landslide-dominated mountain ranges, *Geophys. Res. Lett.*, *35*, L11402, doi:10.1029/2008GL034157.

Larsen, I. J., and D. R. Montgomery (2012), Landslide erosion coupled to tectonics and river incision, *Nat. Geosci.*, doi:10.1038/ngeo1479.

Lebedeva, M. I., R. C. Fletcher, V. N. Balashov, and S. L. Brantley (2007), A reactive diffusion model describing transformation of bedrock to saprolite, *Chem. Geol.*, *244*, 624–645, doi:10.1016/j.chemgeo.2007.07.008.

Lock, J., H. Kelsey, K. Furlong, and A. Woolace (2006), Late Neogene and Quaternary landscape evolution of the northern California Coast Ranges: Evidence for Mendocino triple junction tectonics, *Geol. Soc. Am. Bull.*, *118*, 1232–1246, doi:10.1130/B25885.1.

Mackey, B. H., and J. J. Roering (2011), Sediment yield, spatial characteristics, and the long-term evolution of active earthflows determined from airborne LiDAR and historical aerial photographs, Eel River, California, *Geol. Soc. Am. Bull.*, doi:10.1130/B30306.1.1.

Mackey, B. H., J. J. Roering, and J. A. McKean (2009), Long-term kinematics and sediment flux of an active earthflow, Eel River, Calif., *Geol.*, *37*, 803–806, doi:10.1130/G30136A.1.

Malamud, B. D., D. L. Turcotte, F. Guzzetti, and P. Reichenbach (2004), Landslides, earthquakes, and erosion, *Earth Planet. Sc. Lett.*, *229*, 45–59, doi:10.1016/j.epsl.2004.10.018.

Malet, J. P., and O. Maquaire (2003), Black marl earthflow mobility and long-term seasonal dynamic in southeastern France, in Proceedings of the International Conference on Fast Slope Movements Prediction and Prevention for Risk Mitigation, edited by L. Picarelli, pp. 333–340, Assoiazione Geotechnica Italiana, Pàtron Editore, Bologna.

Marden, M., C. Mazengarb, A. Palmer, K. Berryman, and D. Rowan (2008), Last glacial aggradation and postglacial sediment production from the non-glacial Waipaoa and Waimata Catchments, Hikurangi Margin, North Island, New Zealand, *Geomorphology*, *99*, 404–419, doi:10.1016/j.geomorph.2007.12.003.

Matsukura, Y., and K. Mizuno (1986), The influence of weathering on the geotechnical properties and slope angles of mudstone in the Mineoka earth-slide area, Japan, *Earth Surf. Process. Landforms*, *11*, 263–273.

Mazengarb, C., and I. G. Speeden (2000), Geology of the Raukumara area, Institute of Geological and Nuclear Sciences 1:250,000 geological map 6, 1 sheet and 60 pp., Lower Hutt, New Zealand, Institute of Geological and Nuclear Sciences.

McKean, J. A., W. E. Dietrich, R. C. Finkel, J. R. Southon, and M. W. Caffee (1993), Quantification of soil production and downslope creep rates from cosmogenic ^{10}Be accumulations on a hillslope profile, *Geology*, *21*, 343–346.

McLaughlin, R. J., S. D. Ellen, M. C. J. Blake, A. S. Jayko, W. P. Irwin, K. R. Aalto, G. A. Carver, and S. H. J. Clark (2000), Geology of the Cape Mendocino, Eureka, Garberville, and Southwestern Part of the Hayfork 30×60 Minute Quadrangles and Adjacent Offshore Area, Northern California, U.S. Geological Survey Miscellaneous Field Studies Map MF-2336, 1:100 000 scale.

Milliman, J. D., and J. P. M. Syvitski (1992), Geomorphic/tectonic control of sediment discharge to the ocean: The importance of small mountainous rivers, *J. Geol.*, *100*, 525–544.

Montgomery, D. R., and E. Foufoula-Georgiou (1993), Channel network source representation using digital elevation models, *Water Resour. Res.*, *29*, 3925–3934.

Montgomery, D. R., and M. T. Brandon (2002), Topographic controls on erosion rates in tectonically active mountain ranges, *Earth Planet. Sci. Lett.*, *201*, 481–489, doi:10.1016/S0012-821X(02)00725-2.

National Research Council (2010), Landscapes on the Edge: New Horizons for Research on Earth's Surface, pp. 29–89, The National Academies Press, Washington, DC.

O'Callaghan, J. F., and D. M. Mark (1984), The extraction of drainage networks from digital elevation data, *Comput. Vision Graph. Image Process.*, *28*, 323–344.

Oerlemans, J., and C. J. van der Veen (1984), *Ice Sheets and Climate*, pp. 67–69, D. Reidel Publishing Company, Dordrecht, Holland.

Ollier, C. (1969), Weathering, pp. 21–22, Oliver & Boyd, Edinburgh.

Parker, R. N., A. L. Densmore, N. J. Rosser, M. de Michele, Y. Li, R. Huang, S. Whadcoat, and D. N. Petley (2011), Mass wasting triggered by the 2008 Wenchuan earthquake is greater than orogenic growth, *Nat. Geosci.*, *4*, 449–452, doi:10.1038/NGEO1154.

Payne, A. J., and P. Dongelmans (1997), Self-organization in the thermomechanical flow of ice-sheets, *J. Geophys. Res.*, *102*, 12,219–12,233.

Pelletier, J. D. (2008), *Quantitative Modeling of Earth Surface Processes*, 92–93, Cambridge University Press, Cambridge, UK.

Perron, J. T., W. E. Dietrich, and J. W. Kirchner (2008a), Controls on the spacing of first-order valleys, *J. Geophys. Res.*, *113*, F04016, doi:10.1029/2007JF000977.

Perron, J. T., J. W. Kirchner, and W. E. Dietrich (2008b), Spectral signatures of characteristic spatial scales and nonfractal structure in landscapes, *J. Geophys. Res.*, *113*, F04003, doi:10.1029/2007JF000866.

Pyles, M. R., K. Mills, and G. Saunders (1987), Mechanics and stability of the Lookout Creek earth flow, *Bull. Assoc. Eng. Geol.*, *XXIV*, 267–280.

Rempe, D. M., and W. E. Dietrich (2012), A bottom-up approach to determining the vertical extent of the weathered bedrock zone under ridge and valley topography, Abstract EP43E-03 presented at the 2012 Fall Meeting, AGU, San Francisco, Calif., 3–7 Dec.

Rempe, D. M. J. W. E. Oshun, R. Salve Dietrich, and Fung I. (2010), Controls on the weathering front depth on hillslopes underlain by mudstones and sandstones, Abstract EP34A-05 presented at the 2010 Fall Meeting, AGU, San Francisco, Calif., 13–17 Dec.

Roering, J. J., J. W. Kirchner, and W. E. Dietrich (1999), Evidence for non-linear, diffusive sediment transport on hillslopes and implications for landscape morphology, *Water Resour. Res.*, *35*, 853–870, doi:10.1029/1998WR900090.

Roering, J. J., J. T. Perron, and J. W. Kirchner (2007), Functional relationships between denudation and hillslope form and relief, *Earth Planet. Sc. Lett.*, *264*, 245–258, doi:10.1016/j.epsl.2007.09.035.

Roering, J. J., L. L. Stimely, B. H. Mackey, and D. A. Schmidt (2009), Using DInSAR, airborne LiDAR, and archival air photos to quantify landsliding and sediment transport, *Geophys. Res. Lett.*, *36*, L19402, doi:10.1029/2009GL040374.

Rutt, I. C., M. Hagdorn, N. R. J. Hulton, and A. J. Payne (2009), The Glimmer community ice sheet model, *J. Geophys. Res.*, *114*, F01004, doi:10.1029/2008JF001015.

Salve, R., D. M. Rempe, and W. E. Dietrich (2012), Rain, rock moisture dynamics, and the rapid response of perched groundwater in weathered, fractured argillite underlying a steep hillslope, *Water Resour. Res.*, *48*, W11528, doi:10.1029/2012WR012583.

Savage, W., and J. Wasowski (2006), A plastic flow model for the Acquara-Vadoncello landslide in Senerchia, Southern Italy, *Eng. Geol.*, *83*, 4–21, doi:10.1016/j.enggeo.2005.06.024.

Scheingross, J. S., B. M. Minchew, B. H. Mackey, M. Simons, M. P. Lamb and S. Hensley (2013), Fault-zone controls on the spatial distribution of slow-moving landslides, *Geol. Soc. Am. Bull.*, doi:10.1130/B30719.1.

Schmidt, K. M., and D. R. Montgomery (1995), Limits to relief, *Science*, *270*, 617–620, doi:10.1126/science.270.5236.617.

Schulz, W. H., J. W. Kean, and G. Wang (2009a), Landslide movement in southwest Colorado triggered by atmospheric tides, *Nat. Geosci.*, *2*, 863–866, doi:10.1038/NGEO659.

Schulz, W. H., J. P. McKenna, J. D. Kibler, and G. Biavati (2009b), Relations between hydrology and velocity of a continuously moving landslide-evidence of pore-pressure feedback regulation landslide motion?, *Landslides*, *6*, 181–190, doi:10.1007/s10346-009-0157-4.

Schwab, M., D. Rieke-Zapp, H. Schneider, M. Liniger, and F. Schlunegger (2008), Landsliding and sediment flux in the Central Swiss Alps: A

photogrammetric study of the Schimbrig landslide, Entlebuch, *Geomorphology*, *97*, 392–406, doi:10.1016/j.geomorph.2007.08.019.
Selby, M. J. (1993), *Hillslope Materials and Processes*, pp. 252–258, Oxford University Press, Oxford.
Small, E. E., R. S. Anderson, and G. S. Hancock (1999), Estimates of the rate of regolith production using ^{10}Be and ^{26}Al from an alpine hillslope, *Geomorphology*, *27*, 131–150.
Smith, T. R., and F. P. Bretherton (1972), Stability and the conservation of mass in drainage basin evolution, *Water Resour. Res.*, *8*, 1506–1529, doi:10.1029/WR008i006p01506.
Smolarkiewicz, P. K. (1983), A simple positive definite advection scheme with small implicit diffusion, *Mon. Weather Rev.*, *111*, 479–486.
Stark, C. P., and F. Guzzetti (2009), Landslide rupture and the probability distribution of mobilized debris volumes, *J. Geophys. Res.*, *114*, F00A02, doi:10.1029/2008JF001008.
Stephenson, W. J., and R. M. Kirk (2000), Development of shore platforms on Kaikoura Peninsula, South Island, New Zealand: II: The role of subaerial weathering, *Geomorphology*, *32*, 43–56, doi:10.1016/S0169-555X(99)00062-8.
Strozzi T., P. Farina, A. Corsini, C. Ambrosi, M. Thüring, J. Zilger, A. Wiesmann, U. Wegmüller, and C. Werner (2005), Survey and monitoring of landslide displacements by means of L-band satellite SAR interferometry, *Landslides*, *2*, 193–201, doi:10.1007/s10346-005-0003-2.
Swanson, F. J., and D. N. Swanston (1977), Complex mass-movement terrains in the western Cascade Range, Oregon, *Rev. Eng. Geol.*, *3*, 113–124.
Swanston D. N., R. R. Ziemer, and R. J. Janda (1995), Rate and mechanisms of progressive hillslope failure in the Redwood Creek basin, northwestern California, in Geomorphic Processes and Aquatic Habitat in the Redwood Creek Basin, Northwestern California, edited by K. M. Nolan, H. M. Kelsey, and D. C. Marron, *U.S. Geological Survey Professional Paper* 1454, pp. E1–E16, United States Government Printing Office, Washington, D.C.
Tarboton, D. G. (1997), A new method for the determination of flow directions and upslope areas in grid digital elevation models, *Water Resour. Res.*, *33*, 309–319.
Tarboton, D. G., R. L. Bras, and I. Rodriguez-Iturbe (1991), On the extraction of channel networks from digital elevation data, *Hydrol. Proc.*, *5*, 81–100.
Tarolli, P., and G. D. Fontana (2009), Hillslope-to-valley transition morphology: New opportunities from high resolution DTMs, *Geomorphology*, *113*, 47–56, doi:10.1016/j.geomorph.2009.02.006.
Torrence, C., and G. P. Compo (1997), A practical guide to wavelet analysis, *Bull. Am. Meteorol. Soc.*, *79*, 61–78.
Travelletti, J. and J.-P. Malet (2012), Characterization of the 3D geometry of flow-like landslides: A methodology based on the integration of heterogeneous multi-source data, *Eng. Geol.*, *128*, 30–48, doi:10.1016/j.enggeo.2011.05.003.
Trotter, C. M. (1993), Weathering and regolith properties at an earthflow site, *Q. J. Eng. Geol.*, *26*, 163–178, doi:10.1144/GSL.QJEGH.1993.026.003.02.
Tucker, G. E., and R. L. Bras (1998), Hillslope processes, drainage density, and landscape morphology, *Water Resour. Res.*, *34*, 2751–2764.
Tucker, G. E., and G. R. Hancock (2010), Modelling landscape evolution, *Earth Surf. Processes*, *35*, 28–50, doi:10.1002/esp.1952.
Turcotte, D. L., and G. Schubert (2002), *Geodynamics, 2nd ed*., 311–312, Cambridge University Press, New York.
van der Beek, P., and J. Braun (1999), Controls on post-mid-Cretaceous landscape evolution in the southeastern highlands of Australia: Insights from numerical surface process models, *J. Geophys. Res.*, *104*, 4945–4966.
Vulliet, L. (2000), Natural slopes in slow movement, in Modeling in Geomechanics, edited by M. Zaman, J. R. Booker, and G. Gioda, pp. 654–676, John Wiley & Sons, Chichester, UK.
Vulliet, L., and K. Hutter (1988a), Continuum model for natural slopes in slow movement, *Geotechnique*, *38*, 199–217.
Vulliet, L., and K. Hutter (1988b), Set of constitutive models for soils under slow movement, *J. Geotech. Eng.-ASCE*, *114*, 1022–1041.
Vulliet, L., and K. Hutter (1988c), Viscous-type sliding laws for landslides, *Can. Geotech. J.*, *25*, 467–477.
Wheatcroft, R. A., and C. K. Sommerfield (2005), River sediment flux and shelf sediment accumulation rates on the Pacific Northwest margin, *Cont. Shelf Res.*, *25*, 311–332, doi:10.1016/j.csr.2004.10.001.
Whipple, K. X., and G. E. Tucker (1999), Dynamics of the stream-power incision model: Implications for height limits of mountain ranges, landscape response timescales, and research needs, *J. Geophys. Res.*, *104*, 17661–17674.
Willgoose, G., R. L. Bras, and I. Rodriguez-Iturbe (1991), A coupled channel network growth and hillslope evolution model, 1. Theory, *Water Resour. Res.*, *27*, 1671–1684, doi:10.1029/91WR00935.
Zhang, X., C. J. Phillips, and M. Marden (1991), Internal deformation of a fast-moving earthflow, Raukumara Peninsula, New Zealand, *Geomorphology*, *4*, 145–154.
Zhang, X., C. Phillips, and M. Marden (1993), A comparison of earthflow movement mechanisms on forested and grassed slopes, Raukumara Peninsula, North Island, New Zealand, *Geomorphology*, *6*, 175–187.